


















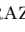





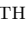
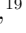





Power-law Emission-line Wings and Radiation-Driven Superwinds in Local Lyman Continuum Emitters

LENA KOMAROVA ¹, M. S. OEY ², RUI MARQUES-CHAVES ³, RICARDO AMORÍN ⁴, ALAINA HENRY ⁵,
DANIEL SCHAEERER ³, ALBERTO SALDANA-LOPEZ ⁶, ALEXANDRA LE RESTE ⁷, CLAUDIA SCARLATA ⁷,
MATTHEW J. HAYES ⁶, OMKAR BAIT ⁸, SANCHAYEETA BORTHAKUR ⁹, CODY CARR ¹⁰, JOHN CHISHOLM ¹¹,
HARRY C. FERGUSON ⁵, VITAL GUTIERREZ FERNANDEZ ², BRIAN FLEMING ¹², SOPHIA R. FLURY ¹³,
MAURO GIAVALISCO ¹⁴, ANDREA GRAZIAN ¹⁵, TIMOTHY HECKMAN ¹⁶, ANNE E. JASKOT ¹⁷, ZHIYUAN JI ¹⁴,
GÖRAN ÖSTLIN ⁶, LAURA PENTERICCI ¹⁸, SWARA RAVINDRANATH ⁵, TRINH THUAN ¹⁹, JOSE M. VÍLCHEZ ⁴,
GABOR WORSECK ²⁰ AND XINFENG XU ²¹

¹*Departament d'Astronomia i Astrofísica, Universitat de València, C. Dr. Moliner 50, E-46100 Burjassot, València, Spain*

²*Astronomy Department, University of Michigan, 1085 South University Avenue, Ann Arbor, MI 48109, USA*

³*Department of Astronomy, University of Geneva, 51 Chemin Pegasi, 1290 Versoix, Switzerland*

⁴*Instituto de Astrofísica de Andalucía (CSIC), Apartado 3004, 18080 Granada, Spain*

⁵*Space Telescope Science Institute, 3700 San Martin Drive, Baltimore, MD, 21218, USA*

⁶*Department of Astronomy, Oskar Klein Centre, Stockholm University, AlbaNova University Centre, SE-106 91 Stockholm, Sweden*

⁷*Minnesota Institute for Astrophysics, School of Physics and Astronomy, University of Minnesota, 316 Church str SE, Minneapolis, MN 55455, USA*

⁸*SKA Observatory, Jodrell Bank, Lower Withington, Macclesfield, SK11 9FT, UK*

⁹*School of Earth & Space Exploration, Arizona State University, Tempe, AZ 85287, USA*

¹⁰*Center for Cosmology and Computational Astrophysics, Institute for Advanced Study in Physics Zhejiang University, Hangzhou 310058, China*

¹¹*Department of Astronomy, University of Texas at Austin, Austin, TX 78712, United States*

¹²*Laboratory for Atmospheric and Space Physics, Boulder, Colorado, United States*

¹³*Institute for Astronomy, University of Edinburgh, Royal Observatory, Edinburgh, EH9 3HJ, UK*

¹⁴*Department of Astronomy, University of Massachusetts Amherst, Amherst, MA 01002, United States*

¹⁵*INAF-Osservatorio Astronomico di Padova, Vicolo dell'Osservatorio 5, I-35122, Padova, Italy*

¹⁶*Department of Physics and Astronomy, Johns Hopkins University, Baltimore, MD 21218, USA*

¹⁷*Astronomy Department, Williams College, Williamstown, MA 01267, USA*

¹⁸*INAF, Osservatorio Astronomico di Roma, via Frascati 33, I-00078 Monteporzio Catone, Italy*

¹⁹*Astronomy Department, University of Virginia, Charlottesville, VA 22904, USA*

²⁰*Institut für Physik und Astronomie, Universität Potsdam, Karl-Liebknecht-Str. 24/25, D-14476 Potsdam, Germany*

²¹*Department of Physics and Astronomy, Northwestern University, 2145 Sheridan Road, Evanston, IL, 60208, USA*

Submitted to The Astrophysical Journal

ABSTRACT

We investigate broad emission-line wings, reaching $\leq 800 \text{ km s}^{-1}$, observed in 26 galaxies with Lyman continuum (LyC) observations, primarily from the Low-redshift Lyman Continuum Survey (LzLCS). Using Magellan/MIKE, VLT/X-shooter, and WHT/ISIS high-resolution spectroscopy, we show that this fast gas appears to probe the dominant feedback mechanisms linked to LyC escape. We find that in 14 galaxies, the wings are best fit with power laws of slope $\alpha \sim -3.5$ to -1.6 , with four others best fit by Gaussians of width $\sigma_{\text{BW}} \sim 300 \text{ km s}^{-1}$; the remaining eight show ambiguous wing morphologies. Gaussian wings are found only at low $O_{32} = [\text{O III}]\lambda 5007/[\text{O II}]\lambda 3726, 3729$ and high metallicity, while power-law wings span the full range of these parameters. The general evidence suggests a dual-mode paradigm for LyC escape: radiation-driven superwinds traced by power-law wings and supernova-driven feedback traced by Gaussian wings. For the former, the $< 3 \text{ Myr}$ -old,

pre-supernova stellar population correlates with more luminous, faster winds. The data also show that radiation-driven wind parameters like wind luminosity and power-law slope α depend on the UV luminosity more than the optically thick covering fraction, consistent with “picket-fence” radiative transfer. Observed α values flatten with both escaping LyC luminosity and higher extinction, while still preserving the anticorrelation between these two quantities. Additionally, the differential between red and blue slopes implies that extinction and dense gas are centrally concentrated relative to the wind emission. Overall, our results show that power-law emission-line wings probe LyC-driven winds and LyC escape in metal-poor starbursts.

Keywords: Emission-line galaxies (459) — Galaxy winds (626) — Interstellar line emission (844) — Lyman-alpha galaxies (978) — Starburst galaxies (1570) — Stellar feedback (1602)

1. INTRODUCTION

The epoch of reionization (EoR) at $z > 6$ marked a key transition in our universe’s history from a largely neutral, opaque state to an ionized and transparent one. While the relative contributions of starbursts and active galactic nuclei (AGN) to reionization remain uncertain (Fontanot et al. 2012; Duncan & Conselice 2015; Cristiani et al. 2016; Matsuoka et al. 2018; Grazian et al. 2024), star-forming galaxies remain a principal agent (Robertson et al. 2013, 2015; Finkelstein et al. 2019; Naidu et al. 2020; Matthee et al. 2022; Mascia et al. 2023; Yeh et al. 2023; Matthee et al. 2023; Atek et al. 2024; Simmonds et al. 2024a). However, a critical remaining unknown is the mechanisms that promote the escape of ionizing radiation, or Lyman continuum (LyC), from hydrogen-rich galaxies. On the one hand, photoionization by young massive stars may reduce the neutral hydrogen optical depth, or even result in a density-bounded medium that allows isotropic LyC escape (e.g., Zackrisson et al. 2013; McClymont et al. 2024). Traditionally, the primary feedback mechanism associated with LyC leakage is clearing by large-scale winds resulting from the collective feedback of SNe and stellar winds. Such mechanical feedback produces a hole-ridden, anisotropic ISM geometry, promoting LyC escape through the optically thin chimneys (Heckman et al. 2011; Zastrow et al. 2013; Kimm & Cen 2014; Ma et al. 2015; Reddy et al. 2016; Trebitsch et al. 2017; Gazagnes et al. 2018; Steidel et al. 2018; Ma et al. 2020; Saldana-Lopez et al. 2022; Bait et al. 2024).

However, at low metallicity, characteristic of the early universe (Curti et al. 2023; Nakajima et al. 2023; Sanders et al. 2023; Chemerynska et al. 2024; He et al. 2024), the onset of SNe is expected to be delayed (Heger et al. 2003; Sukhbold et al. 2016). This is because at low metallicity, most of the stars above $20 - 30 M_{\odot}$ (e.g., O’Connor & Ott 2011; Sukhbold et al. 2016) fail to explode, and instead directly collapse into black holes (e.g., Zhang et al. 2008; O’Connor & Ott 2011). Jecmen & Oey (2023) show

that the majority of the mechanical energy input from SN feedback at $Z \lesssim 0.4 Z_{\odot}$ or $12 + \log(\text{O}/\text{H}) \lesssim 8.3$ is not released until 10 Myr into a cluster’s lifetime. The retention of dense gas, in turn, promotes catastrophic cooling of any hot gas, which may suppress adiabatic superwinds in metal-poor starbursts with high gas densities (Silich et al. 2004; Lochhaas & Thompson 2017; Jaskot et al. 2017, 2019; Gray et al. 2019; Danehkar et al. 2021). Therefore, the mechanism that instead may dominate in the most extreme, young, metal-poor starbursts is radiation-driven feedback. Radiation can drive superwinds, where optically thick gas and dust clumps are accelerated directly by photon momentum from star clusters or AGN (Ishibashi & Fabian 2015; Thompson et al. 2015; Thompson & Krumholz 2016; Krumholz et al. 2017; Tomaselli & Ferrara 2021; Flury et al. 2023). A prime example of such systems is the highly ionized, young, and metal-poor ($12 + \log(\text{O}/\text{H}) = 7.9$; Izotov et al. 1997) system Mrk 71-A in NGC 2366, which shows direct evidence of catastrophic cooling (Oey et al. 2017, 2023). In Komarova et al. (2021), we demonstrated that its $\sim 3000 \text{ km s}^{-1}$ emission-line wings can only be explained by LyC and/or Ly α radiation pressure on tiny, dense neutral hydrogen clumps with an extremely low filling factor on the order of $10^{-3} - 10^{-2}$. As the clumps are continually driven to large distances ($\gtrsim 500 \text{ pc}$) from the cluster and high speeds, LyC photons must reach distances on this order, and thus significant quantities likely escape through the inter-clump regions.

Thus, a paradigm of two modes of LyC escape, dictated by the dominant feedback regime, begins to emerge. In the Low-redshift Lyman Continuum Survey (LzLCS; Flury et al. 2022a), the largest sample of local LyC emitters (LCEs) to date, Flury et al. (2022b) see a hint of these two modes in strongly star-forming galaxies. One population of LCEs shows high H β equivalent width (EW), young ages, high $O_{32} = [\text{O III}]\lambda 5007/[\text{O II}]\lambda 3726, 3729$, and low metallicities. The other is characterized by lower EW(H β), older ages,

lower O_{32} , and higher metallicities. The former population may be dominated by radiation feedback, and the latter by mechanical feedback. Carr et al. (2024) and Bait et al. (2024) present further evidence for this scenario, finding that weaker leakers are preferentially older, SN-dominated systems, while stronger LCEs are younger and radiation-dominated. Furthermore, Flury et al. (2024) show that the confluence of both feedback modes, promoted by bursty star formation, may be required for the highest LyC escape fractions.

The above insights into feedback in LzLCS LCEs were derived from a variety of multiwavelength observations and stellar population synthesis modeling, including optical spectroscopy. Another important diagnostic of feedback mechanisms that can be leveraged from these data are broad emission-line wings. These broad wings are observed in [O III] $\lambda 5007$ and Balmer emission lines, and reach $300\text{--}1000\text{ km s}^{-1}$ (Amorín et al. 2012b; Bosch et al. 2019; Hogarth et al. 2020; Amorín et al. 2024). In addition to LzLCS objects, such wings are likewise seen in several extreme Green Peas (GPs) (Jaskot & Oey 2013; Izotov et al. 2016a,b, 2018a,b), which are some of the strongest known LCEs. Importantly, Amorín et al. (2024) showed that the width of the broad wing correlates with the LyC escape fraction $f_{\text{esc}}^{\text{LyC}}$, demonstrating a direct link between feedback and LyC escape. While SN mechanical feedback or turbulent outflows have been suggested to explain these wings (e.g., Hogarth et al. 2020), the exact physical mechanisms that cause them remain unknown. It appears that AGN feedback can be ruled out based on a systematic lack of very high-ionization markers, such as [Ne V], Fe VII], or X-ray emission (Hogarth et al. 2020; Marques-Chaves et al. 2022; Amorín et al. 2024). However, we linked similar broad wings to radiation-driven winds from a young super star cluster (SSC) in Mrk 71, (Komarova et al. 2021), the closest GP analog. Thus, it is of great interest to test whether radiation driving from young SSCs is the underlying mechanism for the broad wings in the LzLCS galaxies and similar LCEs.

The morphology of the broad wings may be a clue to the underlying feedback mechanism. Indeed, Flury et al. (2023) find that the shape of line wings can be directly linked to driving mechanisms, such as ram pressure. On the one hand, the multitude of expanding shells in SN-driven superbubbles can produce complex, asymmetric emission-line profiles comprised of multiple Gaussian components (Castaneda et al. 1990; Roy et al. 1991; Chu & Kennicutt 1994; Rosado et al. 1996). When integrated over the entire nebula, the resulting wing profile is a broad Gaussian (Chu & Kennicutt 1994; Torres-Flores et al. 2013; Firpo et al. 2010), as determined

by the Central Limit Theorem, where the average of many independent contributions approaches a normal distribution. On the other hand, radiation-driven superwinds can produce power-law or exponential broad wings, depending on the gas density profile (Krumholz et al. 2017). This is seen in Mrk 71-A, whose power-law wings are linked to radiation driving, as inferred from its energy and momentum budgets (Komarova et al. 2021). Thus, characterizing the functional form of broad wings in individual galaxies may help distinguish radiation-driven from SN-driven superwinds.

In this paper, following up on the Amorín et al. (2024) result, we investigate the origin of the broad wings of 20 LzLCS galaxies and 6 extreme GPs (Izotov et al. 2016a,b, 2018a,b). To further illuminate how stellar feedback promotes LyC escape, we use the broad-wing properties of the [O III] $\lambda 5007$ emission line, in conjunction with galaxy properties, to test whether power-law emission-line wings are indeed linked to radiation-driven feedback, while Gaussian wings are linked to SN-driven feedback. We then examine the relation of these feedback modes to LyC escape in these local LCEs. In Section 2, we describe our sample and observations, and our analysis in Section 3. We present our results in Section 4, discuss their implications in Section 5, and summarize our conclusions in Section 6.

2. SAMPLE AND OBSERVATIONS

Our sample consists of 20 star-forming galaxies at $z = 0.23 - 0.36$ from the LzLCS (Flury et al. 2022a), for which follow-up high-resolution optical spectra have been obtained, as well as 6 GPs at $z = 0.29 - 0.37$ (Izotov et al. 2016a,b, 2018a,b). The galaxies in the LzLCS were selected from the SDSS and GALEX surveys, targeting the star-forming region of the Baldwin - Phillips - Terlevich (BPT) diagram (Baldwin et al. 1981), and they span a range of O_{32} , UV slope β , and star formation surface densities Σ_{SFR} . We adopt the published data, including stellar and gas properties of these objects from the above studies and previous LzLCS works by Flury et al. (2022a) and Saldana-Lopez et al. (2022). We present these properties in Table 1, where for each galaxy, Column 1 lists the galaxy’s ID from SDSS and Column 2 lists the redshift z . Column 3 gives the absolute magnitude at 1500 Å M_{1500} from stellar population models, uncorrected for dust extinction. Column 4 gives the oxygen abundance $12 + \log(\text{O}/\text{H})$, derived using direct measurement of the nebular electron temperature, and O_{32} is listed in Column 5. The equivalent widths of $\text{H}\beta$ and $\text{Ly}\alpha$ are given in Columns 6 and 7, respectively. Column 8 provides the UV light fraction of < 3 Myr-old stars $f_*(t < 3)$ from (Flury et al.

2024), based on stellar population synthesis models by Saldana-Lopez et al. (2022). Columns 9 and 10 respectively show the nebular extinction $E(B - V)$ derived from the Balmer decrement and UV half-light radius r_{50} measured from the COS acquisition images. The star formation rate derived from $H\alpha$, $SFR_{H\alpha}$, is given in Column 11. The observed LyC luminosity $L_{\text{LyC,obs}}$ and LyC escape fraction $f_{\text{esc}}^{\text{LyC}}$ are given in Columns 12 and 13, respectively. For $f_{\text{esc}}^{\text{LyC}}$, we adopt the values presented by Flury et al. (2022a), based on UV stellar population fits from Saldana-Lopez et al. (2022). Our sample contains 20 confirmed LCEs, with UV LyC escape fractions $f_{\text{esc}}^{\text{LyC}} = 0.2\% - 62\%$, as well as 6 non-leakers with 2σ upper limits $f_{\text{esc}}^{\text{LyC}} \leq 0.06 - 0.98\%$. As shown in Table 1, our combined sample spans a wide range of properties: stellar masses $\log(M_*/M_\odot) = 8.2 - 10.5$, $O_{32} = 1.5 - 27$, and oxygen abundances $\log(O/H) + 12 = 7.6 - 8.4$. We investigate in detail the broad wings of the $[\text{O III}] \lambda 5007$ emission lines in this sample.

For 12 of these galaxies, we use optical spectra obtained with the X-shooter spectrograph on the Very Large Telescope, and those obtained with the Magellan Inamori Kyocera Echelle spectrograph (MIKE; Bernstein et al. 2003) on the Magellan Clay Telescope for 9 galaxies. For the remaining 5 objects, we use spectra from the Intermediate Dispersion Spectrograph and Imaging System (ISIS) on the 4.2 m William Herschel Telescope. Table 2 specifies the instrument used to observe each galaxy in the sample.

The MIKE observations, conducted on 2021 January 17 – 18, and 2022 March 25 – 26, cover the wavelength range $\sim 3300 - 9500 \text{ \AA}$. With the $0.7''$ slit and 2×2 pixel binning, the resolving power was $R \sim 32000$ on the blue side and $R \sim 31000$ on the red, as measured from arc lines. The total exposure times for each object are in the range $3600 - 9000 \text{ s}$. We performed standard reduction steps, including flat-fielding, wavelength calibration, and extraction, using the CarPy pipeline (Kelson et al. 2000; Kelson 2003). To correct for the residual blaze function (Škoda et al. 2008), we fit polynomials to each order after masking all significant features. Basic flux calibration was performed order by order, using spectrophotometric standard stars. We applied secondary flux corrections to the orders covering $[\text{O III}] \lambda 5007$ using the SDSS spectra. We caution that the SDSS aperture is $3''$ while the MIKE aperture is $0.7''$, affecting the accuracy of this flux calibration adjustment; however, we do not expect this to be a significant issue for our sample, as these galaxies are very compact. Since a standard star was not observed during the 2021 run, we flux-calibrated the 2021 observations using only SDSS $[\text{O III}] \lambda 5007$ fluxes, to calibrate the MIKE

order(s) covering this line. To reduce the effect of cosmic rays and bad pixels, we additionally sigma-clipped each spectrum using a threshold of 8σ in 5 \AA windows. Lastly, we clipped the edges with low signal-to-noise (SNR) of each order and median-combined the overlapping regions. In the reduced spectra, we detect the continuum with $\text{SNR} = 2.5 - 7.0$ around $[\text{O III}] \lambda 5007$ in all but one object, J012910+145935.

The X-shooter echelle spectra in the VIS arm ($\lambda_{\text{obs}} = 5595 - 10240 \text{ \AA}$), originally presented by Marques-Chaves et al. (2022), were obtained in 2021 (ESO Program ID 106.215K; PI: Schaerer). The $1.0''$ slit was used, resulting in a resolving power $R \sim 9000$. For 5 of the 12 galaxies, we use the fully calibrated X-shooter dataset detailed in Guseva et al. (2020) (ESO Program ID 102.B-0942; PI: Schaerer). Lastly, the ISIS observing configuration and reduction are described in detail by Hogarth et al. (2020). The spectra (Program P27, PI: Amorín) were obtained with the $0.9''$ slit. The ISIS blue and red arms cover $\sim 4000 \text{ \AA}$ to $\sim 6000 \text{ \AA}$ and $\sim 7200 \text{ \AA}$ to $\sim 8000 \text{ \AA}$, respectively. The resulting resolving power was $R \sim 6000 - 10000$.

3. ANALYSIS

As originally demonstrated by Amorín et al. (2012b), the emission lines of GPs show complex, multi-component profiles, consisting of $1 - 3$ narrow cores plus broad wings. In this work, following Amorín et al. (2024), we define all Gaussian kinematic components as narrow for $\sigma \leq 100 \text{ km s}^{-1}$, and broad for $\sigma > 100 \text{ km s}^{-1}$. The multiple narrow components likely trace distinct star-forming knots that are separated on kpc scales, as is evident from several 2D spectra. To understand the physical mechanisms traced by the broad wings, we study the broad-wing functional form, or morphology, in $[\text{O III}] \lambda 5007$.

To date, broad emission-line wings in GP-like objects have been assumed to consist of one or multiple Gaussian components (Amorín et al. 2012b; Bosch et al. 2019; Hogarth et al. 2020; Amorín et al. 2024). But from a visual inspection of the broad wings many appear to have a power law form (Komarova et al. 2021), as shown in Figure 1. We therefore test whether these high-velocity wings can be described by power laws, as predicted for radiation-driven winds, or whether they are better fit by gaussians, as may be expected for SN-driven, mechanical feedback (Section 1). These wings are separate components from the narrower, gaussian cores originating from the dense starburst H II regions.

Table 1. Sample Properties

| Galaxy | z | M_{1500}^a | $\log(\text{O}/\text{H})$ | O_{32}^b | $\text{EW}(\text{H}\beta)$ | $\text{EW}(\text{Ly}\alpha)$ | $f_*(t < 3)^c$ | $E(B - V)^d$ | r_{50}^e | $\log(\text{SFR}_{\text{H}\alpha})$ | $L_{\text{LyC,obs}}$ | f_{LyC}^f |
|----------------|------|--------------|---------------------------|------------|----------------------------|------------------------------|----------------|--------------|------------|-------------------------------------|-------------------------|--------------------|
| | | | +12 | | \AA | \AA | | | kpc | $M_{\odot} \text{ yr}^{-1}$ | 10^{41} erg/s | |
| J003601+003307 | 0.35 | -18.1 | 7.8 | 13.1 | 160 | 93 | 0.35 | 0.11 | 0.45 | 1.2 | 0.93 | < 0.010 |
| J004743+015440 | 0.35 | -20.2 | 8.0 | 4.5 | 62 | 42 | 0.96 | 0.19 | 0.62 | 1.3 | 13.1 | 0.01 ± 0.01 |
| J011309+000223 | 0.31 | -19.8 | 8.3 | 2.3 | 41 | 31 | 0.62 | 0.22 | 0.63 | 0.6 | 0.87 | 0.01 ± 0.00 |
| J012217+052044 | 0.37 | -19.5 | 7.8 | 7.6 | 87 | 71 | 0.69 | 0.12 | 0.71 | 0.9 | 1.02 | 0.02 ± 0.01 |
| J012910+145935 | 0.28 | -19.6 | 8.4 | 2.2 | 73 | 40 | 0.39 | 0.16 | 0.64 | 1.1 | 0.27 | < 0.006 |
| J081409+211459 | 0.23 | -20.5 | 8.1 | 1.6 | 29 | - | 0.26 | 0.26 | 1.44 | 1.2 | 0.97 | < 0.007 |
| J090146+211928 | 0.30 | -18.5 | 8.2 | 12.6 | 255 | 170 | 0.27 | 0.22 | 0.18 | 1.3 | 0.21 | 0.03 ± 0.01 |
| J091113+183108 | 0.26 | -20.0 | 8.1 | 2.4 | 73 | 53 | 0.75 | 0.25 | 0.44 | 1.4 | 3.07 | 0.02 ± 0.01 |
| J091703+315221 | 0.30 | -20.0 | 8.5 | 2.6 | 51 | 30 | 0.49 | 0.12 | 0.41 | 1.3 | 4.31 | 0.09 ± 0.03 |
| J092532+140313 | 0.30 | -19.8 | 7.9 | 6.5 | 177 | 83 | 0.68 | 0.16 | 0.40 | 1.7 | 2.19 | 0.09 ± 0.03 |
| J095838+202508 | 0.30 | -18.5 | 7.8 | 8.2 | 131 | 68 | 0.39 | 0.13 | 0.49 | 1.2 | 0.24 | 0.02 ± 0.02 |
| J101138+194721 | 0.33 | -18.8 | 8.0 | 27.0 | 237 | 115 | 0.86 | 0.23 | 0.15 | 1.4 | 1.48 | 0.11 ± 0.02 |
| J105331+523753 | 0.25 | -20.9 | 8.25 | 3.4 | 73 | 7 | 0.33 | 0.20 | 0.62 | 1.4 | 1.05 | 0.01 ± 0.00 |
| J113304+651341 | 0.24 | -19.6 | 7.98 | 5.0 | 64 | 37 | 0.50 | 0.15 | 0.70 | 0.9 | 0.90 | 0.02 ± 0.01 |
| J115205+340050 | 0.34 | -20.7 | 8.00 | 5.4 | 198 | 79 | 0.20 | 0.13 | 0.38 | 1.4 | 4.16 | 0.18 ± 0.06 |
| J115449+244333 | 0.37 | -19.2 | 7.65 | 11.5 | 220 | 133 | 0.41 | 0.15 | 0.64 | 1.3 | 5.35 | 0.62 ± 0.24 |
| J115855+312559 | 0.24 | -20.4 | 8.39 | 2.4 | 70 | 49 | 0.44 | 0.19 | 0.55 | 1.3 | 7.23 | 0.06 ± 0.01 |
| J123519+063556 | 0.33 | -18.7 | 8.36 | 5.5 | 86 | 15 | 0.17 | 0.10 | 0.45 | 1.2 | 0.08 | < 0.005 |
| J124423+021540 | 0.24 | -19.8 | 8.16 | 4.8 | 143 | 41 | 0.51 | 0.23 | 1.00 | 1.5 | 0.44 | 0.004 ± 0.003 |
| J124835+123403 | 0.26 | -19.8 | 8.16 | 4.6 | 139 | 97 | 0.26 | 0.10 | 0.33 | 1.2 | 0.69 | 0.04 ± 0.01 |
| J131037+214817 | 0.28 | -19.5 | 8.35 | 2.0 | 52 | 38 | 0.79 | 0.16 | 0.42 | 1.1 | 0.98 | 0.02 ± 0.01 |
| J131419+104739 | 0.30 | -20.4 | 8.33 | 1.5 | 36 | 7 | 0.62 | 0.28 | 0.97 | 1.3 | 0.16 | < 0.001 |
| J134559+112848 | 0.24 | -20.2 | 8.32 | 1.5 | 27 | - | 0.65 | 0.32 | 1.34 | 1.2 | 0.49 | < 0.001 |
| J144010+461937 | 0.30 | -20.7 | 8.21 | 2.4 | 55 | 29 | 0.97 | 0.24 | 0.64 | 1.5 | 0.65 | 0.002 ± 0.001 |
| J144231-020952 | 0.29 | -20.1 | 7.94 | 6.7 | 312 | 129 | 0.32 | 0.14 | 0.42 | 1.6 | 2.34 | 0.12 ± 0.05 |
| J164607+313054 | 0.29 | -19.5 | 8.10 | 5.4 | 126 | 44 | 0.38 | 0.12 | 0.45 | 1.3 | 0.45 | 0.02 ± 0.01 |

Notes.

All values are from [Flury et al. \(2022a\)](#) unless otherwise noted.

^a Absolute magnitude at 1500 \AA from stellar population models, uncorrected for dust extinction.

^b The typical uncertainty is 0.05.

^c Light fraction of < 3 Myr populations from ([Flury et al. 2024](#)) based on multi-component stellar populations fits by [Saldana-Lopez et al. \(2022\)](#).

^d Nebular extinction derived from the Balmer decrement.

^e Half-light NUV radius from HST/COS. The typical uncertainty is 0.15 kpc.

^f LyC escape fraction, determined from UV SED fits.

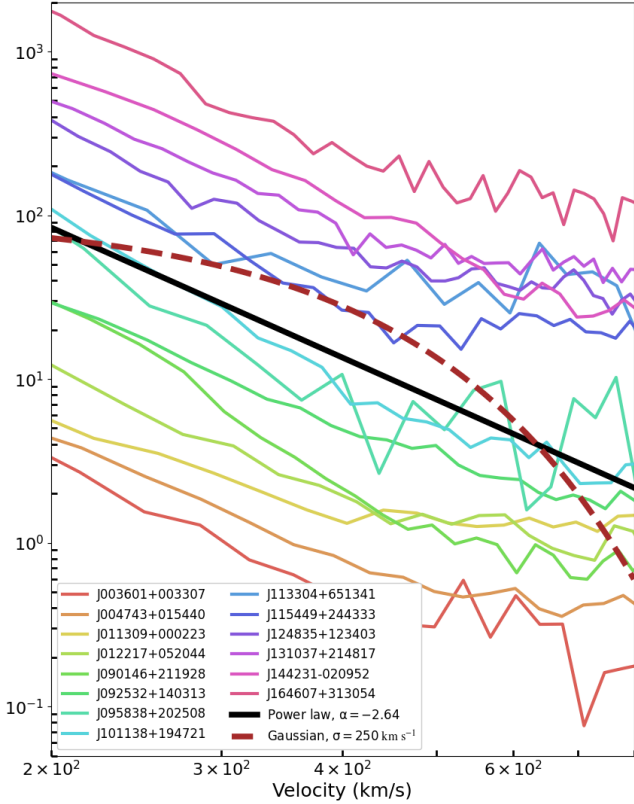


Figure 1. Broad emission-line wings of objects found to be consistent with power-law profiles. The maximum broad-wing extent V_{\max} varies by object and often is less than the x -axis limit of 800 km s^{-1} . This plot shows the blue [O III] $\lambda 5007$ wing with 3-point boxcar binning. The profiles are arbitrarily offset in flux for display purposes. For comparison, a Gaussian (brown dashed line) and the median power-law fit (black solid line) are overlaid.

We first obtain the best Gaussian model for each set of wings, following the fitting procedure of Amorín et al. (2024). Before fitting the wing profiles, we mask out the neighboring contaminating line Fe II $\lambda 5018$ near [O III] $\lambda 5007$. Using the Non-Linear Least-Squares Minimization and Curve-Fitting package LMFIT (Newville et al. 2014), we fit the local continuum in a $\pm 50 \text{ Å}$ window around [O III] $\lambda 5007$ as a constant offset and add additional Gaussian components to each line fit until the Akaike information criterion (AIC, Akaike 1974) does not change significantly ($\Delta \text{AIC} < 10$, Bosch et al. 2019). For this multi-Gaussian fit, we leave free all parameters, i.e., amplitude, centroid, and width σ_{BW} . We perform all spectral fitting in the rest frame of each galaxy.

We then separately find the least-squares power-law fit to the flux F for each object, of the form $F = A \times V^\alpha$, where A is the amplitude, and α is the power-law

slope. Unlike in the simultaneous multi-Gaussian fit, we first isolate the narrow emission of the line core from the wings by fitting a Gaussian for each distinct line peak. We then subtract these core component(s) and define the broad wing as the resulting residuals above $|V| \geq |V_{\min}|$ as shown in Figure 2, where $|V_{\min}|$ is indicated by the vertical dotted lines. The minimum broad-wing velocity V_{\min} corresponds to the velocity at the peak of the core-subtracted residuals. On average, $|V_{\min}| \gtrsim 150 \text{ km s}^{-1}$, though we note that V_{\min} has large uncertainties, as shown by the gray core-wing transition zone in Figure 2. In objects with multiple narrow components, contamination by other star-forming regions may prevent robust disentangling of the wind component at low velocities. We then fit the wings with linear functions in log-log space. We allow the power-law amplitude and slope α to vary between the blue and red side of the wings, denoting these respective slopes as α_{blue} and α_{red} .

It is important to note that our power law models are piece-wise, and do not account for the transition region between the core(s) and the wing, shown in gray in Figure 2, bottom-right panel. We have explored several modifications to the pure power law function, such as truncation or exponential cut-off, but have not found a single universal analytic form that can be fitted simultaneously with the Gaussian cores. Most likely the transition between slow and fast gas cannot be captured by a single analytic form. This kinematic transition must be linked to the wind launch conditions and potentially other factors, such as turbulence, interaction with dense gas components, and geometric effects that differ between galaxies. The wind emission is not expected to extend to the lowest velocities because the denser, low-velocity material is close to the SSC and cannot escape the gravitational potential. Instead, this gas remains bound and contributes to the narrow core near systemic velocity. As shown by Krumholz et al. (2017), this effect results in line profiles consisting of discrete, high-velocity red- and blue-shifted components of the modelled wind emission.

On the other hand, the Gaussian wing models do extend continuously to the lowest velocities. In the SN scenario, this is physically motivated by the existence of multiple dense shell and kinematic structures, with much emission transverse to the line of sight and therefore at zero velocity (Chu & Kennicutt 1994). The two different fitting methods reflect the two different physical models for the origin of the line wings: gaussian line wings must originate from many kinematic components whose sum therefore generates a gaussian function. Gaussians originate from the central limit theorem,

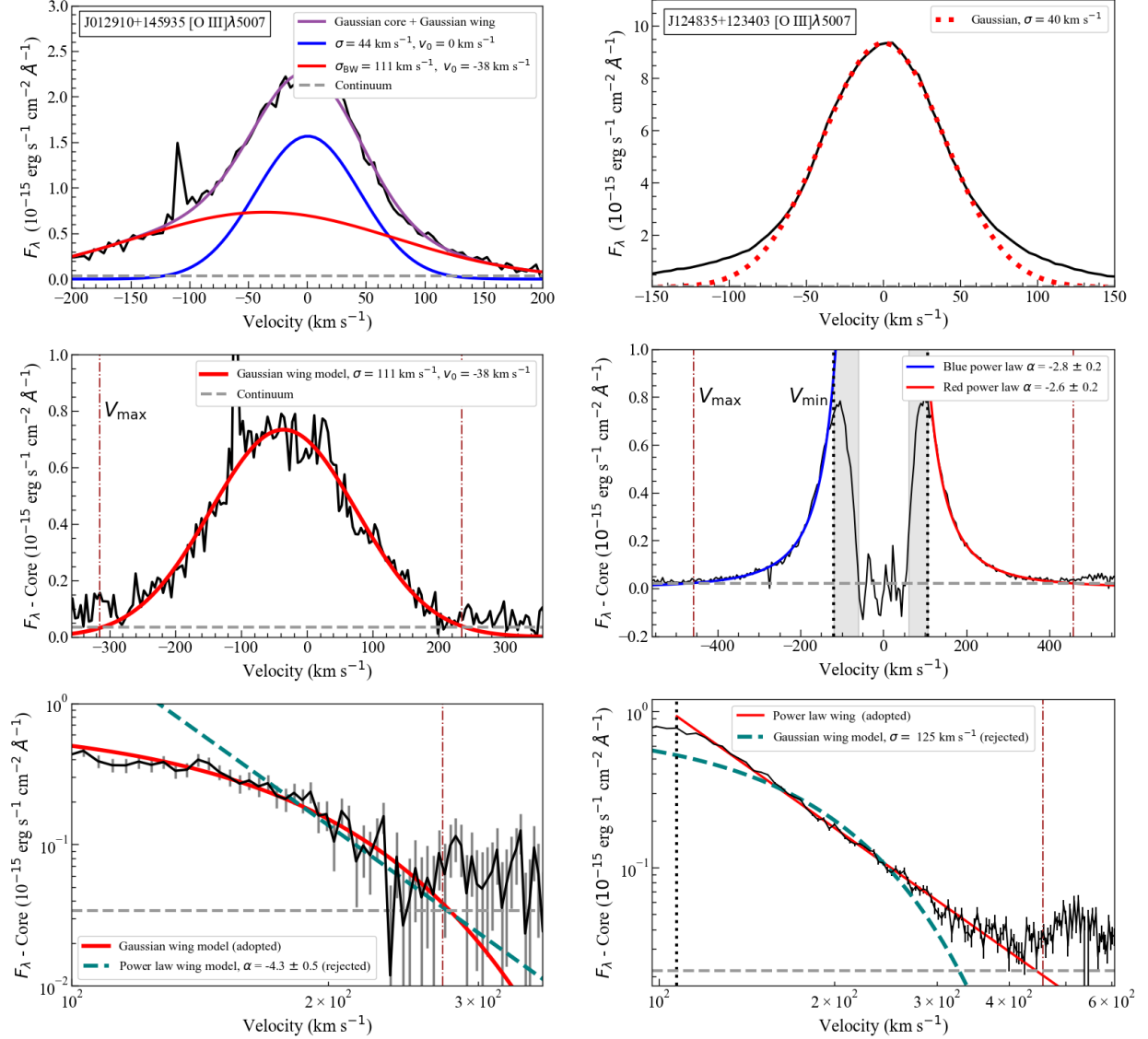


Figure 2. Examples of the two broad-wing model classifications, Gaussian (J012910+145935, left) and power law (J124835+123403, right) in [O III] $\lambda 5007$. The Gaussian models for the narrow line cores are shown in the top panels. In the middle panels, we subtract the core model from the flux and overlay the best-fit wing model. In the bottom panels, we compare Gaussian and power-law models for each set of wings in log-log space. The maximum wing velocity V_{max} is indicated with vertical, purple dash-dotted lines, and the minimum velocity V_{min} of the power-law wings with vertical black dotted lines. Gray regions in the middle-right panel represent the transition regions between the Gaussian core and power-law wings, which are not accounted for in our models; the feature around 500 km s $^{-1}$ is emission from Fe II $\lambda 5018$, which is masked from the fits.

thus the central part of the function is a fundamental component that must be included and accounted for. In contrast, a power law linked to a radially accelerating wind cannot extend to zero velocity and must have a lower limit.

Our objective is to characterize the line wings with simple, physically motivated analytic models that minimize the number of parameters. We therefore select the wing model for a given galaxy with the lower reduced chi-squared χ_r^2 , or χ^2 per degree of freedom, computed over the full extent spanning the red and blue wings.

The power-law models, fitted as linear functions in log-log space, always have four free parameters: a slope and an intercept, or normalization of the power law, for each of the two wings. The Gaussian wing models contain three free parameters, i.e., amplitude, centroid, and width, for each fitted broad Gaussian. We find that for most objects, two narrower Gaussian core components are required, with $\sigma \leq 100$ km s $^{-1}$, in addition to a broad one with $\sigma > 100$ km s $^{-1}$; while for others, one narrow and 1 – 2 broad components are required, consistent with the findings of Amorín et al. (2024). So,

Table 2. [O III] Broad Wing Properties

| Galaxy | Instr. ^a | V_{\max} km s ⁻¹ | $V_{0,\text{wing}}$ km s ⁻¹ | $L_{\geq 300}$ 10 ⁴⁰ erg s ⁻¹ | α_{blue} | α_{red} | σ_{BW} km s ⁻¹ | $\chi^2_{\text{r,G}}$ ^b | $\chi^2_{\text{r,P}}$ ^c | Morph ^d |
|----------------|---------------------|----------------------------------|---|--|------------------------|-----------------------|--|------------------------------------|------------------------------------|--------------------|
| J003601+003307 | Xsh | 524 ± 140 | -17.5 ± 98.9 | 2.99 | -3.1 ± 0.4 | -3.17 ± 0.3 | — | 2.40 | 1.50 | PL |
| J004743+015440 | Xsh | 537 ± 50 | 18.5 ± 35.4 | 10.1 | -2.6 ± 0.1 | -2.21 ± 0.2 | — | 6.80 | 1.30 | PL |
| J011309+000223 | Xsh | 406 ± 50 | 24.5 ± 35.4 | 2.51 | -2.2 ± 0.2 | -1.65 ± 0.1 | — | 1.70 | 1.01 | PL |
| J012217+052044 | Xsh | 543 ± 80 | 19.0 ± 56.6 | 5.94 | -2.3 ± 0.2 | -2.33 ± 0.1 | — | 2.40 | 1.40 | PL |
| J012910+145935 | MIKE | 217 ± 85 | -28.5 ± 60.1 | — | — | — | 118 ± 4 | 1.60 | 2.60 | G |
| J081409+211459 | Xsh | 381 ± 40 | 8.0 ± 28.3 | 5.23 | — | — | — | 3.20 | 1.20 | A |
| J090146+211928 | Xsh | 608 ± 40 | 28.5 ± 28.3 | 3.21 | -3.5 ± 0.1 | -2.60 ± 0.1 | — | 5.70 | 3.50 | PL |
| J091113+183108 | Xsh | 562 ± 40 | 33.0 ± 28.3 | 19.3 | — | — | 350 ± 35 | 0.49 | 0.18 | G |
| J091703+315221 | ISIS | 594 ± 50 | -48.0 ± 35.4 | 22.4 | — | — | — | 0.66 | 0.60 | A |
| J092532+140313 | Xsh | 594 ± 70 | -28.5 ± 49.5 | 8.87 | -2.8 ± 0.2 | -1.67 ± 0.1 | — | 8.60 | 2.70 | PL |
| J095838+202508 | Xsh | 376 ± 40 | 86.5 ± 28.3 | 1.14 | -2.7 ± 0.2 | -2.75 ± 0.2 | — | 2.20 | 0.73 | PL |
| J101138+194721 | Xsh | 771 ± 50 | 48.0 ± 35.4 | 8.92 | -2.8 ± 0.6 | -2.28 ± 0.1 | — | 29.20 | 13.80 | PL |
| J105331+523753 | ISIS | 423 ± 50 | -29.0 ± 35.4 | 1.89 | — | — | 257 ± 40 | 0.36 | 0.26 | G |
| J113304+651341 | ISIS | 413 ± 50 | -20.5 ± 35.4 | 1.84 | -2.3 ± 0.3 | -2.29 ± 0.1 | — | 0.65 | 0.40 | PL |
| J115205+340050 | ISIS | 664 ± 80 | 24.0 ± 56.6 | 36.0 | — | — | — | 0.33 | 0.32 | A |
| J115449+244333 | Xsh | 521 ± 150 | 101 ± 106 | 2.72 | -2.5 ± 0.2 | -1.97 ± 0.2 | — | 2.30 | 1.40 | PL |
| J115855+312559 | MIKE | 490 ± 50 | -47.0 ± 35.4 | 7.49 | — | — | — | 2.37 | 2.41 | A |
| J123519+063556 | MIKE | 520 ± 50 | -37.0 ± 35.4 | 8.75 | — | — | — | 4.97 | 5.00 | A |
| J124423+021540 | MIKE | 470 ± 100 | 62.0 ± 70.7 | 13.3 | — | — | — | 1.65 | 1.57 | A |
| J124835+123403 | MIKE | 414 ± 40 | 13.5 ± 28.3 | 3.69 | -2.8 ± 0.2 | -2.50 ± 0.1 | — | 9.10 | 4.17 | PL |
| J131037+214817 | MIKE | 635 ± 40 | -29.5 ± 28.3 | 8.11 | -2.2 ± 0.1 | -1.96 ± 0.1 | — | 4.30 | 3.50 | PL |
| J131419+104739 | MIKE | 401 ± 50 | -12.0 ± 35.4 | 6.64 | — | — | 352 ± 39 | 2.20 | 3.30 | G |
| J134559+112848 | MIKE | 324 ± 45 | 30.5 ± 31.8 | 1.2 | — | — | — | 2.70 | 1.60 | A |
| J144010+461937 | ISIS | 544 ± 50 | -4.0 ± 35.4 | 5.30 | — | — | — | 0.37 | 0.40 | A |
| J144231-020952 | Xsh | 725 ± 100 | 25.0 ± 70.7 | 12.6 | -2.8 ± 0.1 | -2.18 ± 0.1 | — | 15.30 | 3.40 | PL |
| J164607+313054 | MIKE | 494 ± 45 | 5.0 ± 31.8 | 3.86 | -2.5 ± 0.2 | -2.46 ± 0.1 | — | 3.20 | 1.60 | PL |

Notes.^aSpectrograph used in observations: Magellan/MIKE, VLT/X-shooter, WHT/ISIS.^bReduced χ^2 for the best-fitting Gaussian wing model, computed in the wings.^cReduced χ^2 for the best-fitting power-law wing model, computed in the wings. Gray entries represent unreliable models with dynamic range up to a factor of $< \times 2$.^dWing morphology: power law (PL), Gaussian (G), or ambiguous (A).

the Gaussian wing models contain 3 – 6 free parameters. One caveat is that we reject power-law models with a velocity dynamic range spanning less than a factor of two, regardless of χ^2_{r} . We consider this range to be too short to reliably distinguish between these analytic forms. The cases where the Gaussian vs. power-law models yield similar χ^2_{r} , or neither form satisfactorily reproduces the wing shape, we classify as “ambiguous”. In Figure 2, we show example power-law and Gaussian

wing models. Wing models for all objects are presented in the Appendix of Komarova (2024).

In addition to the morphology, we determine the broad-wing centroid, maximum velocity, and luminosity in each galaxy. We determine the maximum detected broad-wing velocity V_{\max} as the velocity at which the best wing model intersects the local measured continuum on each side of the wing (Figure 2). The values are measured relative to the systemic velocity of the line core as fitted by the gaussian component. The brightest

core is adopted for the systemic velocity if there is more than one core. We then compute the broad-wing centroid velocity $V_{0,\text{wing}}$ as the mid-point of the two V_{max} measurements in the red and blue wings. The instrumental and thermal broadening are $\sim 4 - 10 \text{ km s}^{-1}$ and $\sim 2 \text{ km s}^{-1}$, respectively for [O III] which is small compared to our estimated V_{max} and its uncertainties of $\geq 40 \text{ km s}^{-1}$. Therefore, we do not correct for these small effects. Lastly, we compute the high-velocity luminosity $L_{\geq 300}$ in the wings, by integrating the flux in the range $300 \text{ km s}^{-1} \leq |V| \leq V_{\text{max}}$, i.e., the red and blue emission above 300 km s^{-1} . This velocity threshold ensures a robust, model-independent separation of the wings from the core(s), with the latter extending to $\sim 200 \text{ km s}^{-1}$ in most objects. $L_{\geq 300}$ is undefined for one object in our sample, J012910+145935, which shows $V_{\text{max}} \sim 220 \text{ km s}^{-1}$.

We present our measured broad-wing parameters in Table 2, in addition to the χ_r^2 values for Gaussian and power-law models, and the resulting wing morphology classifications. A complete analysis of line profiles using all observed optical lines will be presented in Amorín et al. (in preparation).

For relating broad-wing parameters to galaxy properties, we use the Kendall's τ rank correlation test as implemented by Flury et al. (2022b) based on Akritas & Siebert (1996). This code accounts for censored data, as required for treatment of upper limits, and estimates confidence intervals for the correlation coefficient τ , based on uncertainties in the correlated parameters, using Monte Carlo sampling. The τ coefficient is a non-parametric measure of the strength and direction of association between two ranked variables, based on the relative ordering of data pairs. It ranges from -1 (perfect anti-correlation) to $+1$ (perfect correlation), with 0 indicating no association. For our full sample of 26 galaxies, we consider a correlation to be significant if the resulting $|\tau| \geq 0.28, p \leq 0.05$, and tentative for $|\tau| \geq 0.24, p \leq 0.1$. When considering the sub-sample of 14 galaxies with power-law wings (Section 4), these respective criteria are $|\tau| \geq 0.41, p \leq 0.05$, $|\tau| \geq 0.36, p \leq 0.1$.

For comparing properties of sub-samples of galaxies, we perform the Kolmogorov-Smirnov (K-S) test, implemented in SciPy. From this test, we quote D , quantifying the maximum difference between two distribution functions, ranging between 0 (no difference) and 1 (maximum difference).

4. RESULTS

We first analyze the full sample of broad emission-line wings, regardless of wing morphology. We consider the broad wing parameters V_{max} , the maximum broad-

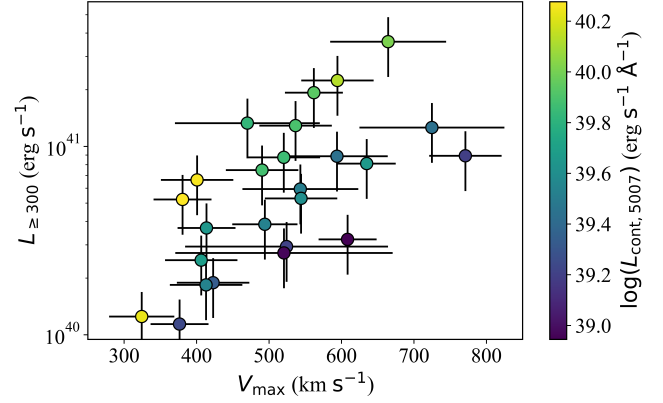


Figure 3. Measured broad wing parameters from [O III] $\lambda 5007$: maximum broad-wing velocity V_{max} vs. luminosity $L_{\geq 300}$, color-coded by 5007 Å median continuum luminosity.

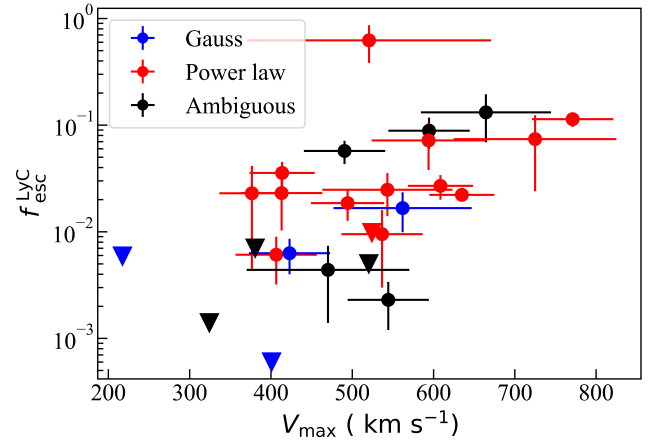


Figure 4. LyC escape fraction $f_{\text{esc}}^{\text{LyC}}$ vs. maximum broad-wing velocity V_{max} in [O III] $\lambda 5007$, color-coded by wing morphology. The triangles represent upper limits on $f_{\text{esc}}^{\text{LyC}}$.

wing velocity, and $L_{\geq 300}$, the high-velocity luminosity. In what follows, we quote the measurements for each parameter as: median (median absolute deviation). The maximum broad-wing velocities V_{max} have a range of $217 - 771 \text{ km s}^{-1}$ with the sample median of $V_{\text{max}} = 520$ (93) km s^{-1} . We obtain broad wing luminosities at $|V| > 300 \text{ km s}^{-1}$ in the range $1.2 \times 10^{40} - 2.8 \times 10^{41} \text{ erg s}^{-1}$, corresponding to 0.6% – 12.4% of the total line luminosity.

To examine the relationship between our measured emission-line wing parameters, we compare V_{max} , $L_{\geq 300}$, and rest-frame 5024 – 5040 Å continuum luminosity $L_{\text{cont}, 5007}$ in Figure 3. The continuum, linked to the galaxy stellar luminosity, is a variable independent of the wind-driving mechanism, but affects our measurements of V_{max} . This SNR effect is seen in Figure 3,

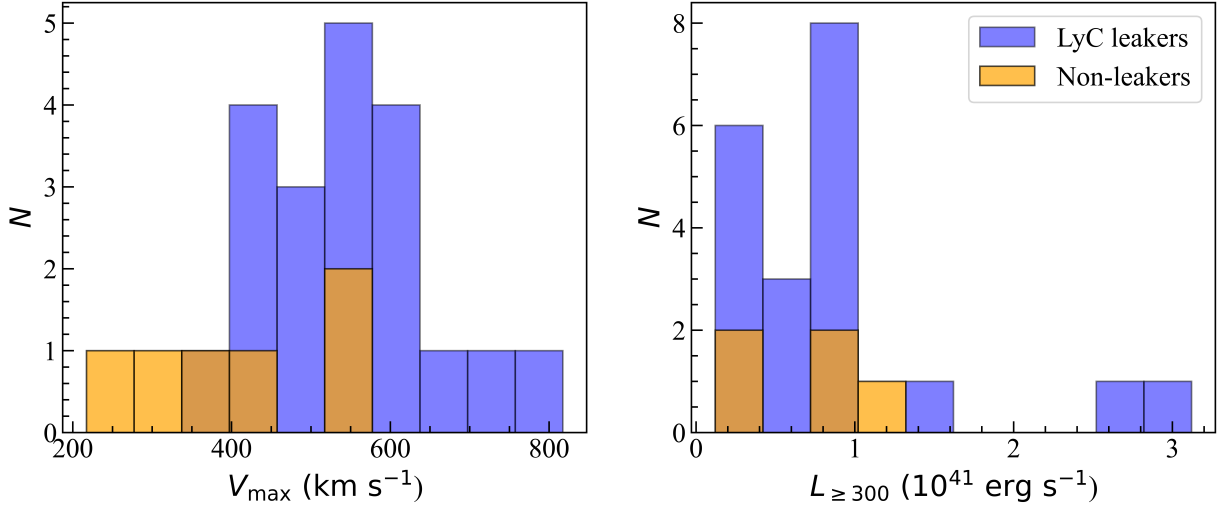


Figure 5. Comparison of V_{\max} and $L_{\ge 300}$ between LyC leakers (blue) and non-leakers (orange).

where objects with higher $L_{\text{cont},5007}$ tend to have lower V_{\max} detections at a given $L_{\ge 300}$.

With the full sample of galaxies considered in this work, we start by reproducing the correlation between the broad-wing velocity and the LyC escape fraction $f_{\text{esc}}^{\text{LyC}}$ established by Amorín et al. (2024), but now with the additional six objects. As shown in Figure 4, we indeed recover this correlation, with our Kendall rank correlation test yielding $\tau = 0.44_{-0.09}^{+0.08}$, $p = 1.6 \times 10^{-3}$. Although we assume varying wing functional forms and use the maximum detected broad-wing velocity V_{\max} rather than the Gaussian width σ_{BW} , our results are consistent with the correlation coefficient obtained by Amorín et al. (2024), $\tau = 0.32_{-0.12}^{+0.10}$, $p = 5.2 \times 10^{-2}$, indicating a correlation of moderate strength.

Our sample contains 20 confirmed LCEs and 6 galaxies without significant ($> 2\sigma$) LyC detections. We compare the maximum broad-wing velocity V_{\max} and high-velocity luminosity $L_{\ge 300}$ for leakers and non-leakers in Figure 5. We find that the sub-sample of LCEs shows higher V_{\max} than the non-LCEs, with the respective median values of 540 (69) km s^{-1} and 390 (98) km s^{-1} . The K-S test yields $D = 0.62$, $p = 3.5 \times 10^{-2}$, rejecting, at the 95% confidence level, the null hypothesis that the two sub-samples originate from the same distribution. This is expected from the V_{\max} - $f_{\text{esc}}^{\text{LyC}}$ correlation discussed above. However, there is no significant difference in the broad-wing luminosity $L_{\ge 300}$ between LCEs and non-LCEs, with the respective median values of 7.6 (3.0) $\times 10^{40} \text{ erg s}^{-1}$ and 7.7 (3.2) $\times 10^{40} \text{ erg s}^{-1}$ and the K-S test resulting in $D = 0.20$, $p = 9.9 \times 10^{-1}$.

We now examine the broad wing morphology. We classify the emission-line wings for 14 of the objects as power-law in form, 4 objects as Gaussian, and 8 as

ambiguous. The power-law wings are characterized by slopes $\alpha = -3.5$ to -1.6 , $V_{\max} = 376 - 771 \text{ km s}^{-1}$, and Gaussian ones by width $\sigma_{\text{BW}} = 118 - 352 \text{ km s}^{-1}$, $V_{\max} = 217 - 562 \text{ km s}^{-1}$. Among the 8 sets of wings with ambiguous wing morphologies, 6 are reasonably well fitted with either model. In the remaining 2 cases, J134559+112848 and J081409+211459, neither power-laws nor Gaussians fit the full extent of the wings well.

Our goal now is to understand the physical origin of the broad emission. The functional form of the broad wings may trace the underlying feedback mechanism responsible for the observed high-velocity gas in each galaxy. In particular, as discussed in Section 1, we suggest that Gaussian broad wings may originate from conventional, SN-driven feedback, and power-law wings from radiation-driven superwinds. To test this hypothesis, we evaluate whether galaxy properties associated with each of the two broad-wing morphologies are consistent with this scenario.

4.1. Power-law vs. Gaussian Emission-line Wings

In Figures 6 and 7, we show how the broad wing morphology relates to O_{32} , $\text{EW}(\text{H}\beta)$, and metallicity. We use the oxygen abundance $12 + \log(\text{O}/\text{H})$ to trace metallicity, and the $\text{H}\beta$ equivalent width $\text{EW}(\text{H}\beta)$ to characterize stellar age. The $\text{EW}(\text{H}\beta)$ traces the contribution of young massive stars producing ionizing emission, relative to the more evolved population dominating the optical continuum. Radiation-driven feedback is expected to be prevalent in younger ($\lesssim 3 \text{ Myr}$) environments with larger $\text{EW}(\text{H}\beta)$, as well as at higher ionization parameters traced by O_{32} , since the ionization parameter probes the ratio of radiation to gas pressure. Radiation feedback is also expected to dominate for longer periods and thus larger population ages for low metallicities, because

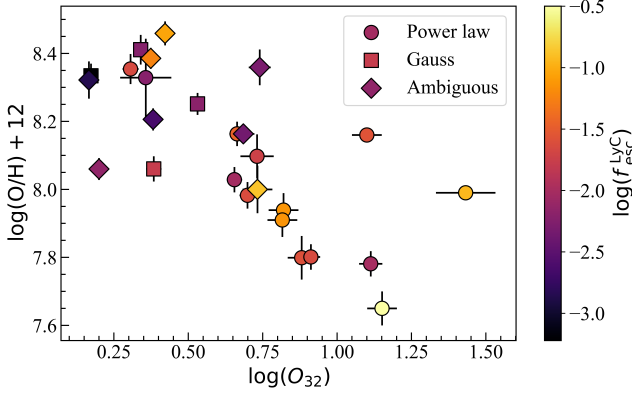


Figure 6. Oxygen abundance vs. $\log(O_{32})$ of the galaxies in our sample, color-coded by $f_{\text{esc}}^{\text{LyC}}$, with different symbols representing the wing morphologies.

the onset of SNe is delayed (Jecmen & Oey 2023). On the other hand, SN feedback is expected to dominate at older stellar ages and higher metallicities, and to generate lower ionization parameters, since gas clearing in the inner region acts to reduce the observed ionization parameter.

We find that Gaussian emission-line wings are found exclusively at lower $O_{32} < 3.5$, higher metallicity $12 + \log(\text{O}/\text{H}) > 8.0$, and lower $\text{EW}(\text{H}\beta) \leq 75 \text{ \AA}$. In contrast, galaxies with power-law wings span the full range of values of these parameters. Importantly, the most extreme starbursts, with $O_{32} > 5.5$, exclusively show power-law wings. These findings are consistent with power-law broad wings being associated with radiation-driven superwinds, and Gaussian wings with SN-driven superwinds, as suggested in Section 1. We do see power-law wings in objects with higher metallicity and low O_{32} , suggesting that radiation-dominated feedback is not limited to low-metallicity conditions, and may be driven primarily by very young, pre-SN ages and intense starbursts. In fact, higher metallicities promote catastrophic cooling (e.g., Danehkar et al. 2021), which is often linked to radiation-dominated feedback.

The galaxies with ambiguous wing morphologies span an intermediate range of properties, showing values similar to those of objects with Gaussian wings, but reaching higher O_{32} and $\text{EW}(\text{H}\beta)$, with $O_{32} \sim 5$ and $\text{EW}(\text{H}\beta) = 200 \text{ \AA}$. Notably, the two galaxies for which neither model satisfactorily reproduces the wing shape, J081409+211459 and J134559+112848, have the lowest O_{32} and $\text{EW}(\text{H}\beta)$ in the sample, with values of ~ 1.5 and $\sim 30 \text{ \AA}$, respectively. As the two weakest line emitters, the low SNR limits our analysis of these objects.

We stress that our sample consists of unresolved galaxies, each likely containing multiple large star-forming regions with varying physical conditions and stellar pop-

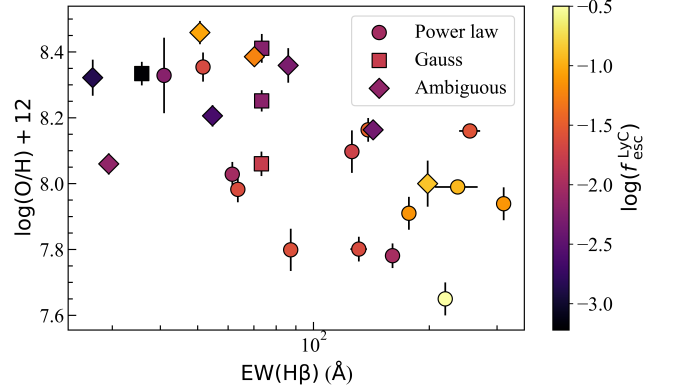


Figure 7. Oxygen abundance vs. $\text{EW}(\text{H}\beta)$, color-coded by $f_{\text{esc}}^{\text{LyC}}$, with different symbols representing the wing morphologies.

ulations, which may include both radiation- and SN-dominated regions. This may explain the overlap in properties of galaxies with Gaussian versus power-law wings. For instance, while all objects with $O_{32} > 5$ show power-law wings and are likely radiation-dominated, we may be seeing a mix of feedback modes at lower O_{32} values, that are driven by different SSCs in the same aperture.

Such diversity of stellar populations and feedback mechanisms is evident in the spatially resolved observations of the closest known LCE, Haro 11, where three star-forming knots with widely differing stellar populations, gas properties, and corresponding feedback and LyC properties are observed (Komarova et al. 2024; Kunth et al. 2003; Adamo et al. 2010; Keenan et al. 2017; Östlin et al. 2021; Le Reste et al. 2024). The integrated galaxy properties of Haro 11 do not trace those of individual knots, for various parameters. For example, the global $O_{32} \sim 3$, significantly lower than that observed in the radiation-dominated region Knot A, where $O_{32} > 9$. Knot A, despite its high O_{32} , is not detected in LyC, and the leaked LyC luminosity is dominated by Knot B, an enshrouded region with the highest intrinsic LyC luminosity. The second leaker Knot C is more optically thin, but has a lower $O_{32} \sim 1$, reducing the galaxy-integrated O_{32} to ~ 3 . If spatially unresolved, Haro 11 would thus be observed in the “composite” region of the parameters space in O_{32} , $\log(\text{O}/\text{H}) + 12$, and $\text{EW}(\text{H}\beta)$, despite hosting two extreme, radiation-dominated knots.

4.2. Radiation Driving of Power-Law Wings

Komarova et al. (2021) used spatially resolved observations of the nearby, radiation-dominated starburst Mrk 71-A to establish the existence of a very thin, clumpy superwind, driven by LyC and/or Ly α photons. This wind is observed as broad, $V_{\text{max}} \gtrsim 3000 \text{ km s}^{-1}$

power-law wings in $[\text{O III}] \lambda 4959, 5007$ and $\text{H}\alpha$ with slope $\alpha \sim -1$. The proximity of Mrk 71, at 3.4 Mpc (Tolstoy et al. 1995), compared to > 1000 Mpc for the GPs, allows a spatially resolved probe into its broad wings. The mass in the broad-wing gas, in combination with the cluster luminosity and observed broad-wing velocity, requires that the wind consist of neutral dense “bullets” with a very low filling factor $\sim 10^{-3} - 10^{-2}$ (Figure 8). The observed wind velocity in Mrk 71-A increases with increasing distance from the cluster, as expected for a radiation-driven wind (e.g., Castor et al. 1975). The wing power-law slope similarly becomes shallower with distance, implying that higher velocity gas dominates there. The broad-wing emission extends to distances $\gtrsim 500$ pc from the cluster, as can be seen from 2-D long-slit spectra published by Gonzalez-Delgado et al. (1994). This suggests that some LyC and/or Ly α photons reach such distances to continue driving the wind, and a fraction of them likely escapes via inter-clump regions (Komarova et al. 2021).

Table 3. Correlations of Broad-Wing Parameters with Galaxy Properties in Objects with Power-Law [O III] Wings

| | V_{\max} | | $L_{>300}$ | | $L_{>300}/L_{\text{tot}}$ | | α_{blue} | | α_{red} | | $\Delta\alpha$ | |
|------------------------------------|--|--|---|--|--|--|---|--|---|--|--|--|
| | τ | p | τ | p | τ | p | τ | p | τ | p | τ | p |
| $f_{\text{LyC}}^{\text{esc}}$ | $0.34_{-0.15}^{+0.15}$ | 9.0×10^{-2} | $0.19_{-0.13}^{+0.13}$ | 3.5×10^{-1} | $0.12_{-0.15}^{+0.15}$ | 5.5×10^{-1} | $-0.24_{-0.13}^{+0.13}$ | 2.3×10^{-1} | $0.10_{-0.15}^{+0.11}$ | 6.2×10^{-1} | $0.27_{-0.15}^{+0.15}$ | 1.7×10^{-1} |
| $f_{\text{Ly}\alpha}^{\text{esc}}$ | $0.05_{-0.13}^{+0.15}$ | 7.8×10^{-1} | $0.16_{-0.11}^{+0.09}$ | 4.1×10^{-1} | $0.23_{-0.13}^{+0.13}$ | 2.5×10^{-1} | $0.18_{-0.11}^{+0.11}$ | 3.8×10^{-1} | $0.38_{-0.11}^{+0.09}$ | 5.5×10^{-2} | $0.30_{-0.13}^{+0.13}$ | 1.4×10^{-1} |
| $L_{\text{LyC,obs}}$ | $0.30_{-0.15}^{+0.15}$ | 1.4×10^{-1} | $0.43_{-0.15}^{+0.13}$ | 3.3×10^{-2} | $0.54_{-0.15}^{+0.13}$ | 7.3×10^{-3} | $0.07_{-0.13}^{+0.13}$ | 7.4×10^{-1} | $0.58_{-0.11}^{+0.11}$ | 3.7×10^{-3} | $0.45_{-0.15}^{+0.13}$ | 2.5×10^{-2} |
| $L_{\text{LyC,abs}}$ | $-0.03_{-0.13}^{+0.11}$ | 8.7×10^{-1} | $0.30_{-0.11}^{+0.11}$ | 1.4×10^{-1} | $0.34_{-0.11}^{+0.13}$ | 8.9×10^{-2} | $0.50_{-0.06}^{+0.09}$ | 1.2×10^{-2} | $0.43_{-0.11}^{+0.11}$ | 3.3×10^{-2} | $0.08_{-0.13}^{+0.13}$ | 7.0×10^{-1} |
| EW(Ly α) | $0.32_{-0.11}^{+0.11}$ | 1.1×10^{-1} | $0.12_{-0.09}^{+0.11}$ | 5.5×10^{-1} | $-0.08_{-0.13}^{+0.13}$ | 7.0×10^{-1} | $-0.57_{-0.02}^{+0.02}$ | 4.4×10^{-3} | $-0.19_{-0.11}^{+0.11}$ | 3.5×10^{-1} | $0.21_{-0.13}^{+0.13}$ | 3.0×10^{-1} |
| EW(H β) | $0.36_{-0.06}^{+0.09}$ | 7.1×10^{-2} | $0.12_{-0.07}^{+0.09}$ | 5.5×10^{-1} | $-0.08_{-0.09}^{+0.11}$ | 7.0×10^{-1} | $-0.66_{-0.02}^{+0.02}$ | 1.0×10^{-3} | $-0.27_{-0.09}^{+0.09}$ | 1.7×10^{-1} | $0.16_{-0.13}^{+0.13}$ | 4.1×10^{-1} |
| SFR | $0.43_{-0.04}^{+0.06}$ | 3.3×10^{-2} | $0.47_{-0.04}^{+0.04}$ | 1.8×10^{-2} | $0.16_{-0.07}^{+0.07}$ | 4.1×10^{-1} | $-0.48_{-0.02}^{+0.02}$ | 1.6×10^{-2} | $0.10_{-0.04}^{+0.07}$ | 6.2×10^{-1} | $0.41_{-0.10}^{+0.10}$ | 4.3×10^{-2} |
| $\Sigma_{\text{SFR,H}\beta}$ | $0.32_{-0.11}^{+0.11}$ | 1.1×10^{-1} | $0.36_{-0.11}^{+0.11}$ | 7.1×10^{-1} | $0.14_{-0.15}^{+0.15}$ | 4.8×10^{-1} | $-0.37_{-0.04}^{+0.06}$ | 6.3×10^{-2} | $-0.10_{-0.15}^{+0.15}$ | 6.2×10^{-1} | $0.03_{-0.15}^{+0.15}$ | 8.7×10^{-1} |
| M_{1500} | $-0.01_{-0.11}^{+0.13}$ | 9.5×10^{-1} | $-0.41_{-0.09}^{+0.11}$ | 4.3×10^{-2} | $-0.34_{-0.11}^{+0.13}$ | 8.9×10^{-2} | $-0.20_{-0.11}^{+0.15}$ | 3.2×10^{-1} | $-0.43_{-0.11}^{+0.11}$ | 3.3×10^{-2} | $-0.30_{-0.13}^{+0.15}$ | 1.4×10^{-1} |
| log(O/H) | $0.05_{-0.13}^{+0.13}$ | 7.8×10^{-1} | $0.12_{-0.11}^{+0.11}$ | 5.5×10^{-1} | $0.27_{-0.15}^{+0.13}$ | 1.7×10^{-1} | $0.20_{-0.13}^{+0.11}$ | 3.2×10^{-1} | $0.12_{-0.09}^{+0.09}$ | 5.5×10^{-1} | $0.16_{-0.15}^{+0.11}$ | 4.1×10^{-1} |
| O_{32} | $0.19_{-0.13}^{+0.13}$ | 3.5×10^{-1} | $-0.10_{-0.11}^{+0.09}$ | 6.2×10^{-1} | $-0.30_{-0.13}^{+0.15}$ | 1.4×10^{-1} | $-0.44_{-0.04}^{+0.02}$ | 2.8×10^{-2} | $-0.32_{-0.15}^{+0.13}$ | 1.1×10^{-1} | $-0.14_{-0.18}^{+0.15}$ | 4.8×10^{-1} |
| $f_*(t < 3)$ | $0.16_{-0.09}^{+0.09}$ | 4.1×10^{-1} | $0.27_{-0.11}^{+0.11}$ | 1.7×10^{-1} | $0.49_{-0.13}^{+0.11}$ | 1.4×10^{-2} | $0.37_{-0.10}^{+0.10}$ | 6.3×10^{-2} | $0.36_{-0.11}^{+0.11}$ | 7.1×10^{-2} | $0.05_{-0.15}^{+0.11}$ | 7.8×10^{-1} |
| $r_{50,\text{UV}}$ | $-0.38_{-0.13}^{+0.13}$ | 5.5×10^{-2} | $-0.27_{-0.13}^{+0.13}$ | 1.7×10^{-1} | $-0.08_{-0.18}^{+0.18}$ | 7.0×10^{-1} | $0.48_{-0.11}^{+0.11}$ | 1.6×10^{-2} | $0.08_{-0.15}^{+0.18}$ | 7.0×10^{-1} | $-0.27_{-0.18}^{+0.18}$ | 1.7×10^{-1} |
| E(B-V) | $0.27_{-0.15}^{+0.13}$ | 1.7×10^{-1} | $0.16_{-0.15}^{+0.13}$ | 4.1×10^{-1} | $0.38_{-0.18}^{+0.15}$ | 5.5×10^{-2} | $0.04_{-0.15}^{+0.18}$ | 8.3×10^{-1} | $0.43_{-0.18}^{+0.15}$ | 3.3×10^{-2} | $0.47_{-0.18}^{+0.18}$ | 1.8×10^{-2} |

NOTE—For each combination of correlated parameters for the sample of 14 objects, we show the Kendall rank correlation coefficient τ and p values. Tentative correlations with $0.05 < p \leq 0.1$ are italicized, and significant correlations with $p \leq 0.05$ are boldfaced.

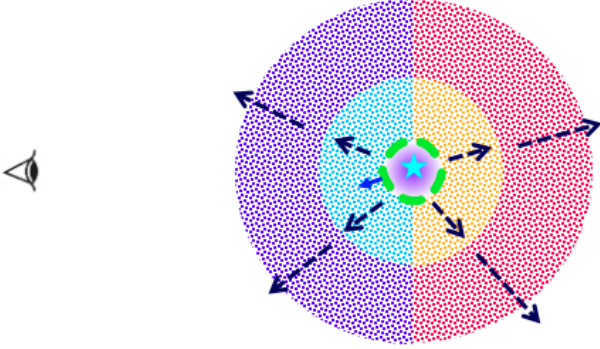


Figure 8. LyC photons escape through gaps in the dense, fragmented shell (green) surrounding the parent cluster and drive a superwind composed of tiny neutral gas clumps with a low filling factor. These radiation-driven wind clumps continue to absorb photons and accelerate, reaching higher speeds at larger radial distances (arrows), corresponding to respectively larger Doppler shifts (red and blue color coding). The dense clouds have a slow, momentum-conserving outward motion driven by the weak stellar winds.

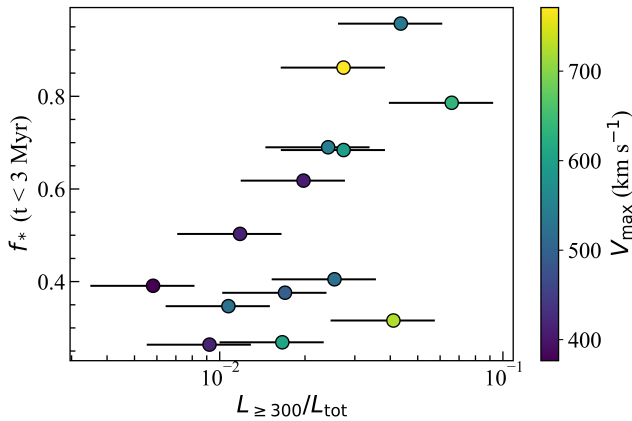


Figure 9. Normalized broad-wing luminosity vs. light fraction of < 3 Myr-old stellar populations, color-coded by V_{\max} .

Stellar radiation feedback occurs in starbursts with young ages and high ionization parameters, where values of $\log(U) \gtrsim -2$ signal that radiation pressure can drive outflows (e.g., Yeh & Matzner 2012). Mrk 71-A, characterized by an age of ~ 1 Myr, $\text{EW}(\text{H}\beta) = 505 \text{ \AA}$, and $O_{32} = 23$ (Micheva et al. 2017), is a strong example of such conditions. The SSC is extremely compact, with a stellar mass of $M_* \sim 10^5 M_\odot$ (Gonzalez-Delgado et al. 1994) and a cluster radius of 1.5 pc (Micheva et al. 2017). Notably, Mrk 71-A hosts very massive stars (VMS, $> 100 M_\odot$) (Smith et al. 2023), making it especially relevant for radiation-driven feedback during its first few million years.

We list the correlations between galaxy properties and power-law wing parameters in Table 3. As shown in Figure 9, we see a significant correlation of relatively brighter wings for objects increasingly dominated by the young, < 3 Myr-old, population ($\tau = 0.49$, $p = 1.4 \times 10^{-2}$). Given that this population is too young to be SN-dominated, this link serves as evidence that the high-velocity gas is due to radiation driving. At subsolar metallicities, where the onset of SNe is delayed and stellar winds are weak, mechanical feedback cannot provide momentum comparable to that from a LyC-driven superwind. From Starburst99 (Leitherer et al. 2014) simulations of a $10^6 M_\odot$ cluster at $Z = 0.004$, close to the mean metallicity of our sample, we see that at 2 Myr, the mechanical momentum input dp/dt is $\sim 5\times$ lower than that from LyC luminosity, based on the mass-loss prescription by Vink et al. (2001). However, more recent studies show that these values are more likely to be overestimated by one to two orders of magnitude (Ramachandran et al. 2019; Rickard et al. 2022; Björklund et al. 2023). Our observations are therefore consistent with LyC radiation dominating the feedback from the young populations observed in this low-metallicity sample, and the scenario that the broad, power-law line wings are a signature of momentum-driven winds.

The radiative transfer of LyC for radiation-dominated feedback is expected to occur via the “picket-fence” geometry (Heckman et al. 2001, 2011; Gazagnes et al. 2018; Steidel et al. 2018; Jaskot et al. 2019; Gazagnes et al. 2020), where LyC escapes via optically thin windows among optically thick clouds (Figure 8). In the LzLCS sample, stronger LyC leakers show higher HI and absorption line residual fluxes for low ionization species (LIS), indicating that LyC likely escapes via low-density paths intermixed with higher-density channels (Saldana-Lopez et al. 2022). We find that the normalized wing luminosity $L_{\ge 300}/L_{\text{tot}}$ correlates with the leaked LyC luminosity $L_{\text{LyC,obs}}$ ($\tau = 0.54$, $p = 7.3 \times 10^{-3}$); however, it does not significantly correlate with the LyC escape fraction $f_{\text{esc}}^{\text{LyC}}$ ($\tau = 0.12$, $p = 5.5 \times 10^{-1}$; Figure 10). This suggests that the wind emission emerges via the same optically thin channels as the LyC radiation in these leakers. The lack of correlation with $f_{\text{esc}}^{\text{LyC}}$ indicates that the emerging wind luminosity is more closely linked to the LyC luminosity than the covering fraction of dense gas, consistent with the LyC-driven model for the wind. Indeed, we find no significant correlations of the fractional wing luminosity with the H I covering fractions C_{HI} derived by Saldana-Lopez et al. (2022) ($\tau = 0.09$, $p = 4.9 \times 10^{-1}$). Thus, these results are fully consistent with LyC driving the wind through

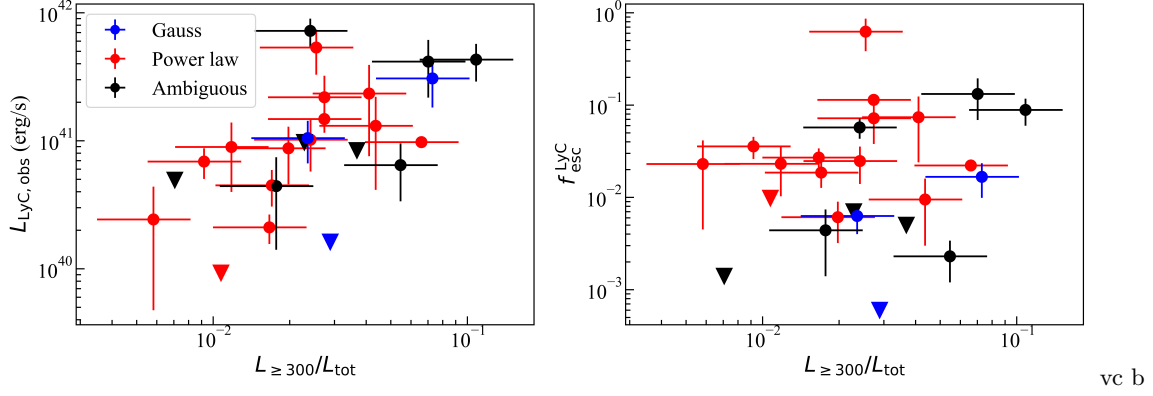


Figure 10. Left: observed LyC luminosity vs. normalized broad-wing luminosity $L_{\geq 300}/L_{\text{tot}}$. Right: LyC escape fraction $f_{\text{esc}}^{\text{LyC}}$ vs. $L_{\geq 300}/L_{\text{tot}}$.

the picket-fence geometry, where both emerge between clouds of dense gas.

4.3. Broad-wing power-law slope and LyC escape

In addition to the broad-wing velocity and luminosity, a fundamental parameter characterizing the power-law wings is the power-law slope α , which also shows trends linked to LyC escape. As we show below, it appears to represent the combination of the intrinsic wind velocity profile and the optical depth structure. As described in Section 3, we measure α independently in the blue and red wings as α_{blue} and α_{red} , respectively. The blue wing originates from the near-side, approaching part of the wind, and the red one from the far side, as illustrated in Figure 8.

Both blue and red slopes appear to be linked to the youngest, UV-dominant population. Both α_{blue} and α_{red} show a tentative correlation with the UV light fraction of < 3 Myr-old stars $f_*(t < 3)$ (blue: $\tau = 0.37$, $p = 6.3 \times 10^{-2}$; red: $\tau = 0.36$, $p = 7.1 \times 10^{-2}$; Table 3). Both slopes are shallower for higher fractions of < 3 Myr stars, suggesting that the wind velocity profile is faster for populations increasingly dominated by the youngest stars. This shared trend therefore suggests that the wing profiles are likely determined largely by the intrinsic wind velocity structure linked to radiation-driving.

Figure 11 shows the relations of α_{blue} and α_{red} to $f_{\text{esc}}^{\text{LyC}}$, as well as to the observed LyC luminosity $L_{\text{LyC,obs}}$, and $f_{\text{esc}}^{\text{Ly}\alpha}$. The figure is color-coded by $f_{\text{esc}}^{\text{LyC}}$, and we see a possible trend where, for a given $f_{\text{esc}}^{\text{LyC}}$, galaxies with stronger $L_{\text{LyC,obs}}$ tend to have higher, flatter values of α_{blue} ; however, there is no such trend between $f_{\text{esc}}^{\text{LyC}}$ and α_{blue} (see also Table 3). This pattern is similar to that seen in Figure 10. It therefore suggests that α is linked directly to the wind luminosity, implying that more luminous winds also have velocity profiles weighted more toward high velocities. This further supports our suggestion in the preceding section that the

wind emission is fundamentally linked to the LyC luminosity, rather than the escape fraction, and consistent with picket-fence radiative transfer.

Thus, our data suggest that stronger, more luminous leakers may tend to have shallower slopes. Such a scenario may be expected in the radiation-driven wind case, since more escaping photons allow prolonged acceleration of the wind to larger velocities, which may lead to an observed velocity profile weighted toward higher values, and hence, a shallower slope. It is less clear whether there is a similar trend with higher $f_{\text{esc}}^{\text{Ly}\alpha}$ (Figure 11). This may imply that LyC, rather than Ly α opacity, dominates the wind acceleration.

4.4. Broad-wing power-law slope and extinction

We find that the red wing is systematically shallower than the blue wing (Table 2), with measured slope differences $\Delta\alpha = \alpha_{\text{red}} - \alpha_{\text{blue}}$ in the range $\sim 0.5 - 1.0$. As shown by Carr et al. (2021), this can be explained by dust extinction. Figure 12 shows the relations of α_{red} , α_{blue} , and $\Delta\alpha$ with the absorbed LyC luminosity $L_{\text{LyC,abso}} = L_{\text{LyC,int}} - L_{\text{LyC,obs}}$, where $L_{\text{LyC,int}}$ and $L_{\text{LyC,obs}}$ are the intrinsic and observed LyC luminosities, respectively; and also with $E(B-V)$ and $12 + \log(\text{O}/\text{H})$. Trends emerge for α_{red} when considering a given $f_{\text{esc}}^{\text{LyC}}$, keeping in mind that $f_{\text{esc}}^{\text{LyC}}$ anticorrelates with extinction (e.g., Saldana-Lopez et al. 2022). The correlations are much weaker for α_{blue} , which is consistent with expectation, given the longer path lengths for redshifted vs blueshifted emission. We find that the slope difference $\Delta\alpha$ also increases with higher dust extinction $E(B-V)$ ($\tau = 0.47$, $p = 1.8 \times 10^{-2}$), as shown in Figure 12 and Table 3, consistent with this scenario. We note that $E(B-V)$ is derived from the nebular Balmer lines rather than UV extinction, and so it may not be especially sensitive to line-of-sight effects probed here.

The relations in Figure 11 show significantly stronger trends for α_{red} than α_{blue} , especially that for $L_{\text{LyC,obs}}$

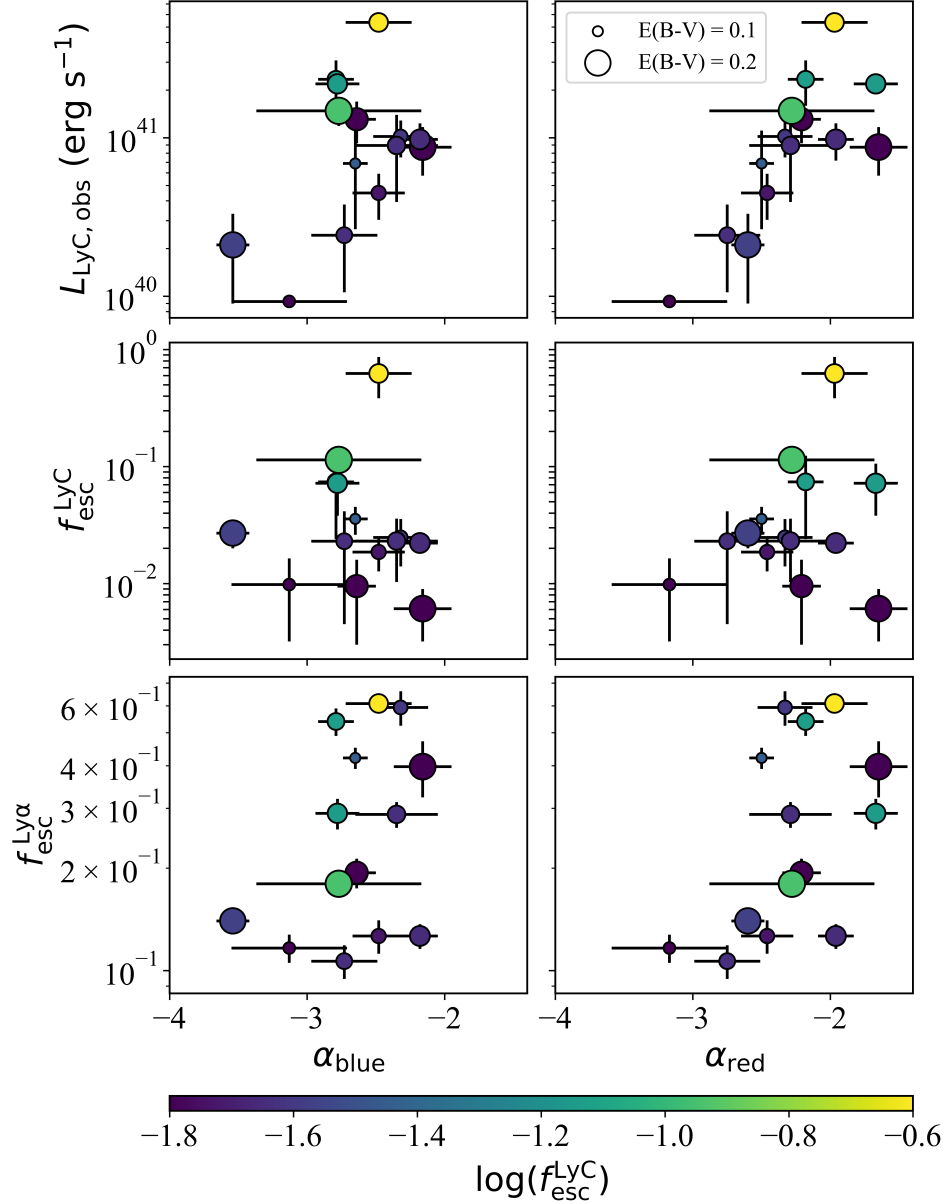


Figure 11. Power-law slopes α_{blue} and α_{red} of the broad emission-line wings vs observed LyC luminosity (top), LyC escape fraction (middle), and Ly α escape fraction (bottom). The points are color-coded by $f_{\text{esc}}^{\text{LyC}}$ and sized by $E(B - V)$.

(see also Table 3). In Figure 11, the size of the points increases with higher $E(B - V)$, demonstrating that the correlations are enhanced in the α_{red} plots largely by the shifted positions of galaxies with higher $E(B - V)$. Thus, the prominent correlations for α_{red} may be somewhat misleading since they are driven in part by extinction.

The fact that α_{red} is shallower with extinction is an important diagnostic of the dust geometry relative to the wind. In Figure 13, we consider four different configurations for the radiative transfer. Their effects on the emission-line profile rely on the expectation that the radiation-driven wind velocity increases with radius, as discussed above (Section 4.2). Figure 13a shows a radi-

ally decreasing power-law density distribution in which the dust is cospatial with the emitting wind. Carr et al. (2021) show that such a model results in a flattening of the red emission-line wing. Figure 13b considers a model where all the extinction originates from the central, compact dusty region, whose radius is much smaller than the extent of the wind. This model is also expected to flatten the slope of the red wing: in both of these models, the centrally concentrated extinction disproportionately attenuates redshifted wind emission originating at smaller, slower radial zones (orange) compared to that from larger, faster ones (red). For a given sightline s , these smaller radial zones correspond to emission ex-

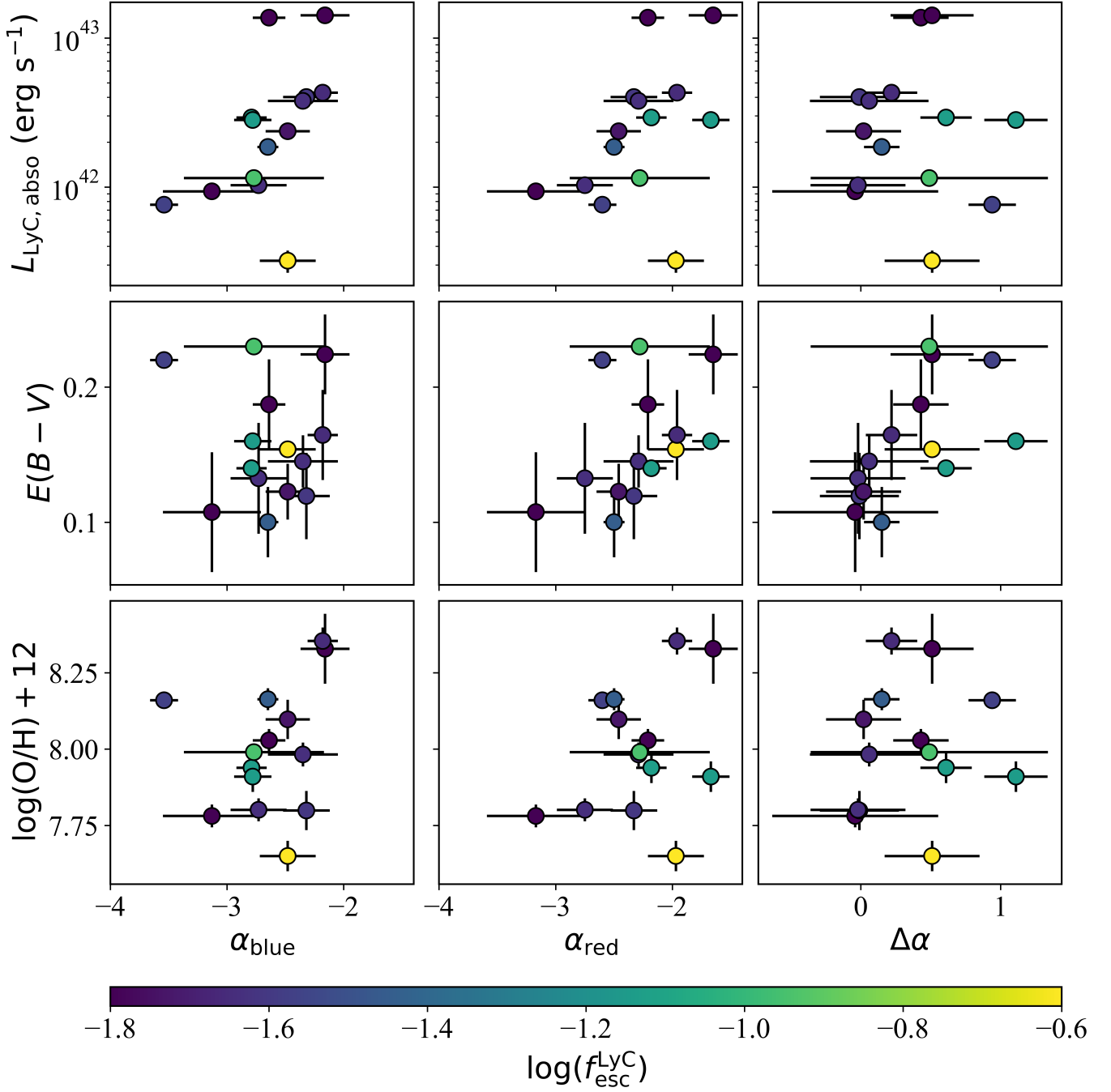


Figure 12. Power-law slopes α_{blue} and α_{red} , and the slope difference $\Delta\alpha$ vs absorbed LyC luminosity (top), $B - V$ color excess (middle), and oxygen abundance (bottom). The points are color-coded by $f_{\text{esc}}^{\text{LyC}}$.

cited by UV originating from a larger range of angles θ , when compared to the contribution from larger radial zones. This results in a greater relative attenuation in luminosity from lower velocity gas, flattening the red slope.

On the other hand, Figure 13c shows dust that is uniformly distributed within the wind volume, rather than centrally concentrated. Here, the extinction is deter-

mined only by the path length in the line of sight. As shown in Figure 13c, for a given sightline, the components contributing from the same radial zone are specified by $|\theta|$. The blueshifted and redshifted path lengths are given by $s_b = s_1$ and $s_r = s_1 + 2s_2$, respectively. We see that the difference $s_r - s_b = 2r \cos \theta$ is largest when $\cos \theta = 1$, and decreases with $\cos \theta$. Therefore, the largest projected velocities experience the greatest

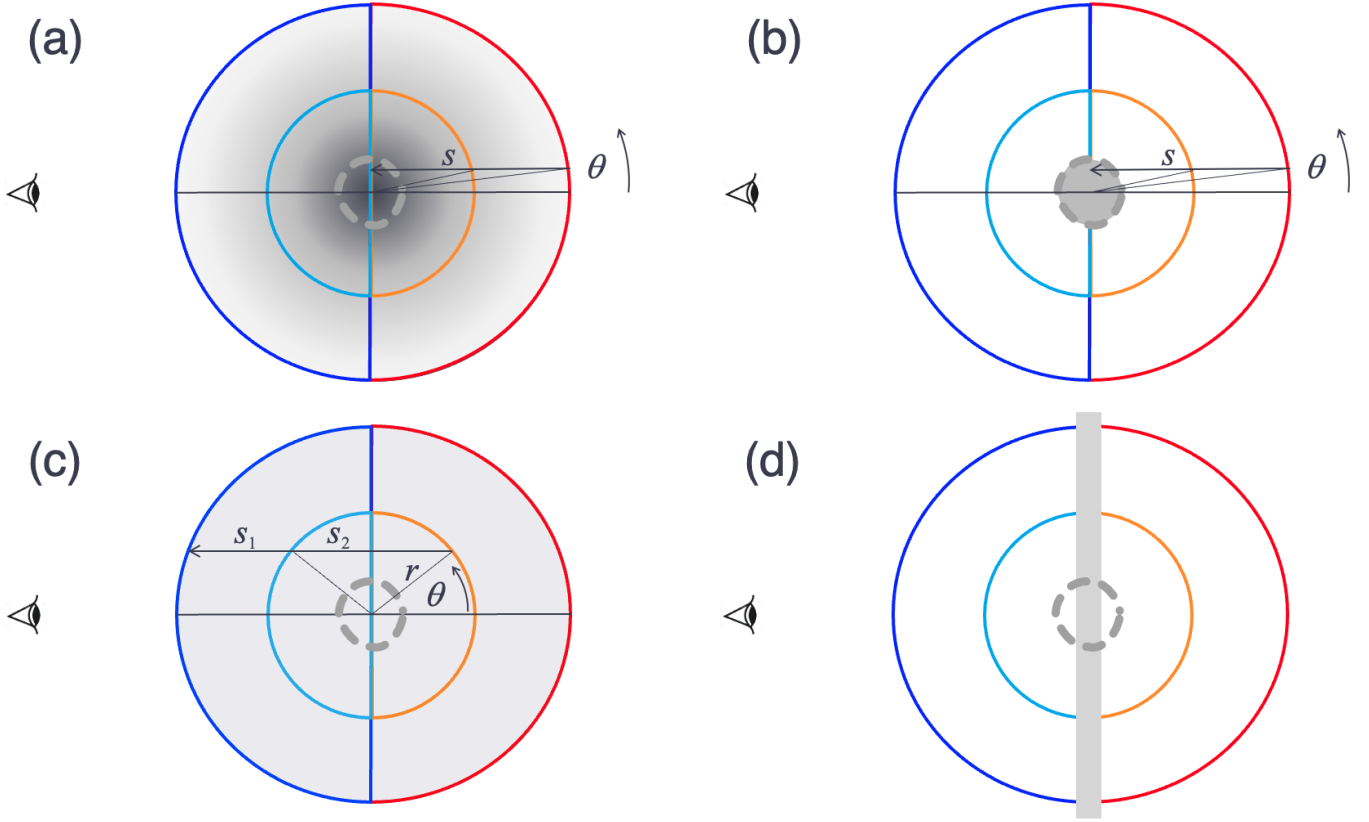


Figure 13. Sketches of different dust configurations (shaded gray). Panel (a) shows a model for centrally concentrated extinction from Carr et al. (2021), and Panel (b) shows one in which extinction originates exclusively from the central dense zone, which is much smaller than the radial extent of the emitting wind. In these two panels, the shown sightline s includes photons emitted from slower gas at smaller radius (orange) and fast gas at large radius (red); these originate from excitation by UV radiation from the SSC emitted over a larger range of θ for slow gas relative to fast gas. Panel (c) shows a model for dust distributed uniformly within the wind volume. For the shown sightline (straight arrow), the blueshifted path length is given by s_1 and the redshifted one by $s_1 + 2s_2$. For the model in Panel (d), the extinction originates from a slab across the center of the system. See text for details on how these models affect the emission-line profiles.

attenuation at all radial zones, implying that the slope of the red emission-line wing steepens. Alternatively, a uniform dust screen through the center of the system and perpendicular to the line of sight (Figure 13d) would attenuate all emission from the red wing uniformly. This would simply reduce the normalization of the red wing luminosity and it would not affect the slope.

Therefore, the observed trend of flatter α_{red} with higher dust extinction points to centrally concentrated extinction as in Figures 13a and 13b. This is consistent with the nature of Green Peas as extremely compact systems where the gas remains close to the ionizing SSC, with LyC radiation escaping through a picket-fence configuration for the dust (e.g., Jaskot et al. 2019). However, we cannot easily distinguish between the two models in Figures 13a and 13b from the red wing flattening alone.

Instead, the behavior of the blue wing slope can help discriminate between these two models. For the

blueshifted emission in Figure 13b, we see that the attenuation is generated only at very small radii, and therefore it is limited to the very lowest velocities. Therefore, the blue slope is largely unchanged. In contrast, in Figure 13a, the dust density tracks the wind density, which would cause some attenuation and some slope flattening for all blueshifted wind material, although not as much as for the redshifted side.

Parameters with strong correlations for α_{blue} are mostly linked to the stellar continuum of the young, UV-bright population, which is directly accessible to our line of sight; this is the side of the wind probed by α_{blue} . There is a general trend that less extreme starbursts with dustier, weaker UV-emitting populations, and which have less LyC leakage in our line of sight, have flatter blue slopes; this trend is opposite to that in Section 4.3 where more luminous LyC emitters show flatter slopes. Table 3 indicates that α_{blue} shows trends with various galaxy parameters that are all con-

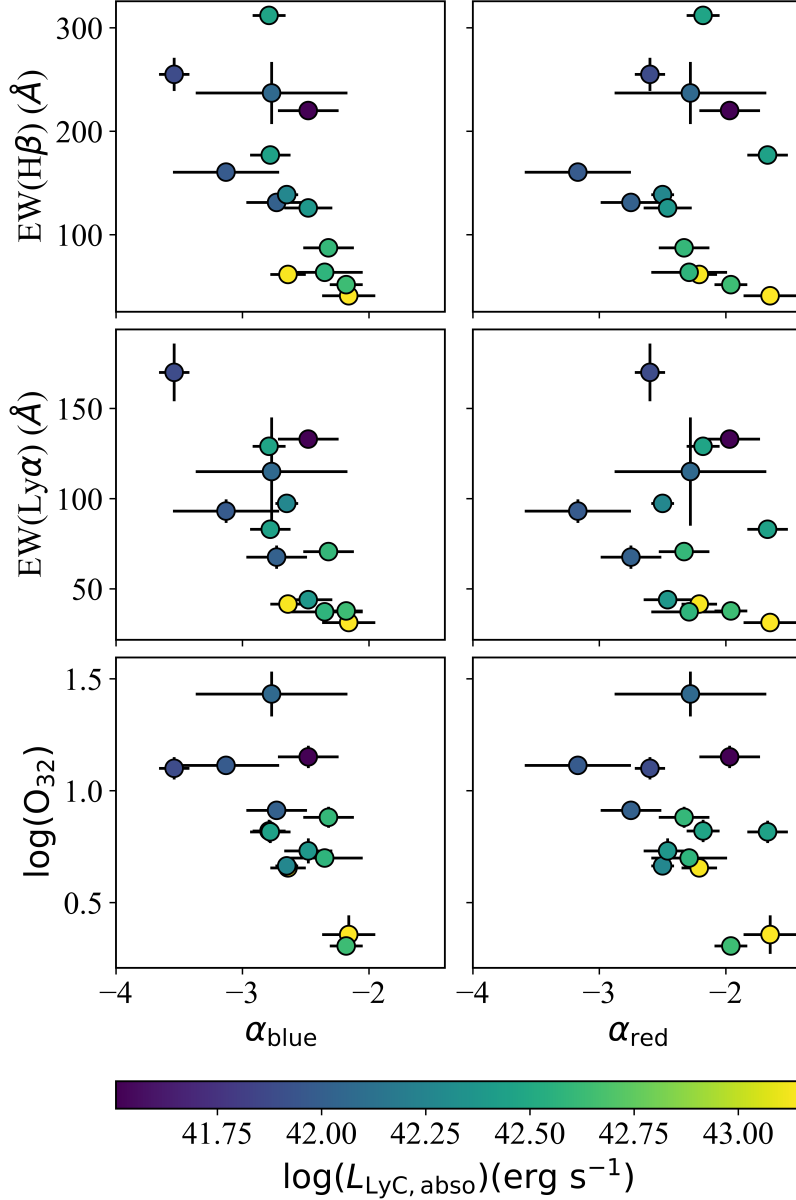


Figure 14. Blue and red wing power-law slopes α_{blue} and α_{red} vs $\text{EW}(\text{H}\beta)$ (top), $\text{EW}(\text{Ly}\alpha)$ (middle), and O_{32} (bottom). The points are color-coded by the absorbed LyC luminosity.

sistent with the blue slope flattening with higher extinction and metallicity (Figure 14): α_{blue} flattens for lower $\text{EW}(\text{H}\beta)$ ($\tau = -0.66$, $p = 1.0 \times 10^{-3}$) and $\text{EW}(\text{Ly}\alpha)$ ($\tau = -0.57$, $p = 4.4 \times 10^{-3}$), and it is also shallower for lower O_{32} ($\tau = -0.44$, $p = 2.8 \times 10^{-2}$) and lower star formation rates ($\tau = -0.48$, $p = 1.6 \times 10^{-2}$). These are all properties that scale with metallicity (e.g., Figures 6 and 7). That this is driven by galaxy scaling relations is supported by the correlation of α_{blue} with larger UV half-light radii r_{50} ($\tau = 0.48$, $p = 1.6 \times 10^{-2}$), confirming that larger galaxies have flatter slopes. Similarly, the red slope α_{red} anticorrelates with M_{1500} ($\tau = -0.43$, $p = 3.3 \times 10^{-2}$). As shown in Figure 12, the

lack of significant correlations between the wing slopes and $12 + \log(\text{O}/\text{H})$ suggests that metallicity itself is not the principal driver. Instead, as shown above, total extinction appears to be more relevant. Figure 14 shows that objects with low O_{32} and $\text{H}\beta$ equivalent width have absorbed LyC luminosities that are an order of magnitude higher than the ones with high O_{32} and $\text{EW}(\text{H}\beta)$. Indeed, both the blue and red slopes have significant correlations with $L_{\text{LyC, abso}}$ (blue: $\tau = 0.50$, $p = 1.2 \times 10^{-2}$; red: $\tau = 0.43$, $p = 3.3 \times 10^{-2}$) as seen in Figure 12.

The sensitivity of the α_{blue} to extinction therefore favors the model for dust distribution in Figure 13a (Carr et al. 2021) rather than Figure 13b. *The dust appears to*

be distributed with a centrally concentrated density profile that is consistent with occupying much of the wind volume. It may even be that the wind material itself is responsible for self-absorption of its emission; further study is needed to determine whether this is reasonable.

Overall, we therefore see that flatter power-law slopes correspond to both stronger radiation-driven winds linked to higher LyC escape and also higher dust extinction. However, it is important to note that this does *not* mean that dustier objects have stronger LyC escape, which would contradict findings in the literature (e.g., Saldana-Lopez et al. 2022; Flury et al. 2022b). The color coding in Figure 12 shows that for any given value of α and $\Delta\alpha$, $f_{\text{esc}}^{\text{LyC}}$ tends toward lower values of $E(B - V)$ and $12 + \log(\text{O}/\text{H})$, as expected.

Extinction can also explain why many parameters that correlate with α_{blue} in Table 3 do not correlate with α_{red} , and vice versa: underlying correlations for α_{blue} are distorted by extinction for α_{red} , while non-correlations in α_{blue} are often driven to a correlation in α_{red} that reflects the amount of extinction. As noted above, Figures 11 and 12 show that the points shifting the most between plots for α_{blue} vs α_{red} are those with high extinction.

4.5. Broad-wing systemic velocity offset

For the sample with power-law line wings, our data show a systematic offset between the systemic velocity of the broad wing component and the bright line core, such that the broad wing systemic velocity $V_{0,\text{wing}}$ is redshifted relative to that of the line core $V_{0,\text{core}}$ (Figure 15). We find that this offset reaches values of $V_{0,\text{wing}} - V_{0,\text{core}} \sim +100 \text{ km s}^{-1}$, with a median value of 18.7 km s^{-1} . Although individual errors are large, the standard error of the median is 14.5 km s^{-1} ; while the standard error generally applies to measurements of a single value, the fact that it is less than the offset here suggests that the latter is statistically significant.

The sample redshifted offset appears to be robust despite multiple factors counteracting such an effect. As described in Section 3, $V_{0,\text{wing}}$ is calculated as the central velocity between the blue and red V_{max} for each object. We also recalculated $V_{0,\text{wing}}$ as the flux centroid between the wings, in case our interpretation of extinction to the red wing is incorrect. The systematically redshifted offsets of $V_{0,\text{wing}}$ relative to $V_{0,\text{core}}$ remain for the flux centroids, despite the red wing attenuation. As shown by Carr et al. (2021), the centrally-concentrated extinction model determined in Section 4.4 causes the peak of the line profile to become blueshifted. This explains the finding by Amorín et al. (2024) that the broad wings are systematically blueshifted relative to the cores, instead of redshifted: that work models the broad wing compo-

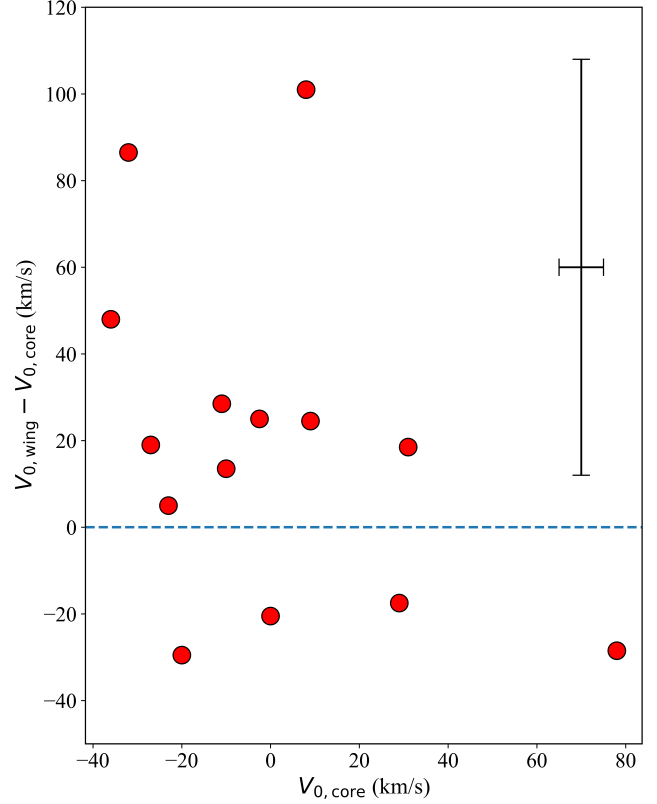


Figure 15. Velocity offset $V_{0,\text{wing}} - V_{0,\text{core}}$ between the systemic velocities of the [O III] broad wings and line core vs the core systemic velocity $V_{0,\text{core}}$, for the power-law wing sample. A representative error bar is shown in the top-right corner.

nent with symmetric Gaussians, whereas we have seen that the red wings are fainter and shallower than the blue ones; a symmetric Gaussian fitted to such a profile becomes systematically blueshifted. We also expect the largest redshifted velocities to suffer the highest attenuation, reducing V_{max} for the red wing. To illustrate, for a fully optically thick cloud whose radius is 20% (50%) that of the emitting wind in Figure 13b, the largest permitted sightlines correspond to 0.98 (0.87) $\times V_{\text{max}}$. The fact that we obtain persistent redshifts for the broad-wing systemic velocity despite these effects suggests that the systematic offset is robust in our dataset.

This systematic offset also may be interpreted as a blueshift of the core relative to the large-scale wind. One possible explanation is that the bright core component could originate from a dense, fragmented stellar wind-driven shell in the line of sight (Figure 8). Stellar winds in metal-poor, pre-SN, radiation-dominated starbursts are weak, but still expected to exist and will generate momentum-driven outflows rather than energy-driven ones (e.g., Jecmen & Oey 2023; Danekhar et al. 2021). Such a dense, $\sim 20 \text{ pc}$ shell is spatially resolved in

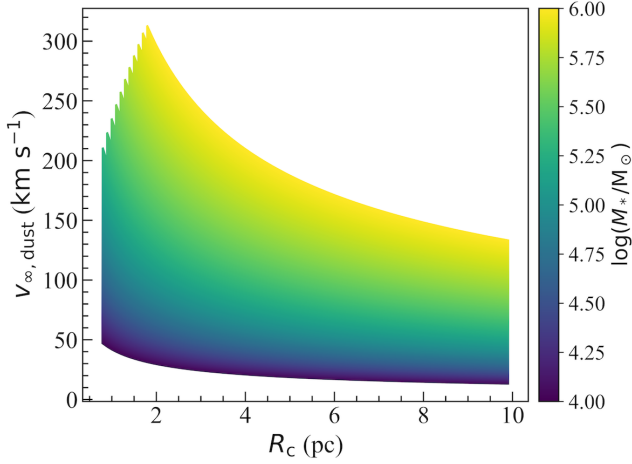


Figure 16. Terminal velocity $v_{\infty,\text{dust}}$ of a radiation-driven superwind, accelerated by a cluster with radius R_c , mass M_* , and M_*/L_* ratio of Mrk 71-A, assuming dust opacity $\kappa = 10^3 \text{ cm}^2 \text{ g}^{-1}$ (Eq. 1). We limit the displayed cluster parameter combinations to those that do not exceed the maximum stellar density $\Sigma < 10^5 \text{ M}_{\odot} \text{ pc}^{-2}$.

the central region of Mrk 71, causing the bright core nebular emission to be blue-shifted by 12 km s^{-1} in [O III] with respect to the surrounding gas at larger radii (Komarova et al. 2021). With high extinction in the line of sight, the observed bright line core from the central region could be strongly dominated by its blueshifted component.

Another effect that may or may not be related is the offset between the systemic Ly α emission and optical nebular emission reported by Orlitová et al. (2018) for a sample of Green Pea galaxies. The latter is defined by core line emission, which is similarly found to be blueshifted relative to the Ly α modeled systemic velocity by values of $10 - 250 \text{ km s}^{-1}$. The cause of this effect is unknown. It may be that the systemic velocity offset between the [O III] core and broad-wing components is another manifestation of this phenomenon.

4.6. Opacity of Radiation-Driven Superwinds

Constraining the driving opacity of radiation-driven superwinds in our sample in principle requires knowledge of individual SSC and feedback parameters within each galaxy. In particular, the terminal velocity v_{∞} of the radiation-driven superwind produced by a cluster with mass M_* , luminosity L_* , and escape velocity v_{esc} is given by (Krumholz et al. 2017; Komarova et al. 2021):

$$v_{\infty} = \sqrt{\frac{L_* \kappa}{4\pi G M_* c} - 1} \times v_{\text{esc}} \quad , \quad (1)$$

where κ is the opacity of the wind material. Thus, from known cluster properties, the observational lower limit on $v_{\infty} \sim V_{\text{max}}$ can be linked to κ .

We evaluate the possibility of dust driving by comparing the predicted dust-driven velocity to the observed values. Assuming the cluster $L_*/M_* \sim 260 L_{\odot}/M_{\odot}$ of Mrk 71-A (Komarova et al. 2021), and the UV dust opacity $\kappa = 10^3 \text{ cm}^2 \text{ g}^{-1}$ (Draine 2003), we obtain the range of maximum dust velocities shown in Figure 16. We consider the parameter space with cluster radii $R_c = 1 - 10 \text{ pc}$ and cluster masses $M_* = 10^4 - 10^6 \text{ M}_{\odot}$, limited by the upper limit on stellar density $\Sigma < 10^5 \text{ M}_{\odot} \text{ pc}^{-2}$, beyond which radiation pressure will disrupt the cluster (Crocker et al. 2018). The highest velocity that dust can produce in this cluster parameter space, even assuming such extreme radiation fields as in Mrk 71-A, is $\sim 300 \text{ km s}^{-1}$. However, all the galaxies we classify as radiation-dominated show $V_{\text{max}} \geq 376 \text{ km s}^{-1}$ (Table 2). While there are some circumstances in which UV dust opacity may reach values up to $10 - 100\times$ higher than assumed in our fiducial model (Draine 2003), the link between the power-law wing slope and luminosity to the absorbed LyC luminosity argues that LyC driving is more likely.

4.7. SN-driven feedback

As we have seen, our results show that SN feedback is more likely to dominate in the subset of our sample galaxies with Gaussian broad wings (Section 4.1). These objects have higher metallicities and lower ionization parameters, consistent with expectations that SNe are more prevalent at higher metallicity and older ages (e.g., Jecmen & Oey 2023). Mechanical feedback is known to generate gaussian line profiles in observed systems, e.g., 30 Dor (Chu & Kennicutt 1994), which originate from the superposition of many expanding shells.

While our results support the existence of UV-driven superwinds in the objects with power-law emission-line wings, such line profiles may not necessarily be exclusively linked to radiation driving. Moreover, observed core nebular line profiles from energy-driven feedback are often known to be irregular and more strongly asymmetric, as is also observed for some of our power-law sample (e.g., Shopbell & Bland-Hawthorn 1998; Xu et al. 2024). For example, multiphase, high-resolution hydrodynamic simulations show that 10^4 K gas entrained in a hot, energy-driven wind can similarly show radially increasing velocities in a mature, $\sim 30 \text{ Myr}$ -old, M82-like starburst (e.g., Schneider et al. 2020; Schneider & Mao 2024). It is possible that such gas could also show broad, power-law wings similar to those in our sample. The preceding sections demonstrate that the ages, momen-

tum budget, and other parameters preclude this scenario in some of our power-law sample, but it remains possible that the power-law wings for some higher-metallicity galaxies could originate from mechanical, rather than radiative, feedback. Another possible mechanism for obtaining a power-law profile for SN-driven feedback is turbulent mixing layers on the surfaces of cool gas clumps interfacing with a hot adiabatic wind (Binette et al. 2009; Eggen et al. 2021). But in general, velocities in excess of $\sim 200 \text{ km s}^{-1}$ are not expected from turbulence, unless driven by AGN (Ulivi et al. 2024), and the same age restrictions for SN-driven superwinds apply.

4.8. $\text{Ly}\alpha$ Emission and Feedback

We use measurements of the spatially resolved $\text{Ly}\alpha$ emission from the Lyman-alpha and Continuum Origins Survey (LaCOS; Le Reste et al., in preparation.) The LaCOS survey is an HST/ACS imaging program (Program ID 17069, PI: Hayes; archival data from Program ID 14131, PI: Orlitová and Program ID 11107, PI: Heckman) for 42 of the 66 total LzLCS galaxies, in a filter set that includes SBC/F150LP and F165LP. In the redshift range $0.23 < z < 0.32$, these two filters cover $\text{Ly}\alpha$ line emission and local UV continuum, respectively. The aim of the survey is to map ISM properties and $\text{Ly}\alpha$ radiative transfer in LyC leakers and non-leakers. For 13 galaxies cross-matched between LaCOS and our sample, we analyze the radii containing 20% and 80% of the $\text{Ly}\alpha$ flux, denoted $r_{20,\text{Ly}\alpha}$ and $r_{80,\text{Ly}\alpha}$, respectively. These radii were measured in apertures $1.5\times$ the Petrosian radius (Petrosian 1976), using StatMorph (Rodríguez-Gomez et al. 2019), after continuum subtraction. These radii and their ratio characterize the spatial concentration of $\text{Ly}\alpha$ emission. We relate these to broad-wing parameters regardless of wing morphology, as there are only six objects with power-law wings and completed LaCOS measurements.

As shown in Figure 17, there may be a trend between the compactness of $\text{Ly}\alpha$ emission traced by the ratio $r_{80,\text{Ly}\alpha}/r_{20,\text{Ly}\alpha}$, and the broad-wing velocity V_{max} over the sample of available objects. However, there is a noticeable outlier, J105331+523753, that has an unusually compact $\text{Ly}\alpha$ halo compared to the rest of the sample. As these values are preliminary, it is unclear whether this might be due to a measurement issue. We quantify its status by calculating the Cook’s distance $D_C = 0.32$, which slightly exceeds the standard threshold of $4/n = 0.31$, qualifying it as an influential outlier. When including this object, the sample in Figure 17 shows no significant correlation ($\tau = -0.10$, $p = 4.5 \times 10^{-1}$); however, excluding the outlier, the Kendall test results in a significant anti-correlation, with $\tau = -0.48$, $p = 2.8 \times 10^{-2}$.

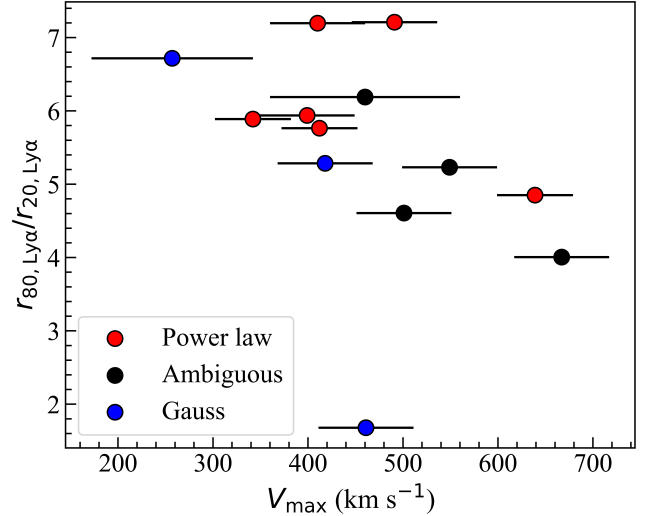


Figure 17. Ratio of the radii enclosing 80% and 20% of the flux in $\text{Ly}\alpha$ vs. V_{max} , color-coded by wing morphology.

Thus, we tentatively suggest that more compact $\text{Ly}\alpha$ emitters may have faster outflows. We saw earlier that galaxies with higher V_{max} also tend to be stronger LyC leakers (Figure 10), and Saldana-Lopez et al. (in preparation) indeed confirm that more compact $\text{Ly}\alpha$ emitters have higher $f_{\text{esc}}^{\text{LyC}}$. This is reasonable since smaller $\text{Ly}\alpha$ radii suggest less scattering and thus more direct LyC and $\text{Ly}\alpha$ escape. LyC leakers are associated with lower HI content (e.g., McKinney et al. 2019; Gazagnes et al. 2020) which also lead to less $\text{Ly}\alpha$ scattering. We do not distinguish between SN- and radiation-driven superwinds here, but Figure 17 suggests that the trend seems to apply to both modes of feedback. This is especially the case if the “ambiguous” objects include contributions from both.

Our findings thus allow a first glance into the possible link between $\text{Ly}\alpha$ morphology and stellar feedback in confirmed local LCEs; additional results will be presented by Le Reste et al. (in preparation) and Saldana-Lopez et al. (in preparation).

5. DISCUSSION

5.1. A New Paradigm for LyC Escape

In the classical paradigm of LyC escape, SN feedback promotes the leakage of ionizing photons by expelling neutral gas and clearing out optically thin pathways in the ISM (e.g., Heckman et al. 2011; Zastrow et al. 2013; Kimm & Cen 2014; Ma et al. 2015; Trebitsch et al. 2017; Steidel et al. 2018; Barrow et al. 2020; Saldana-Lopez et al. 2022). However, in the early universe and other metal-poor environments, radiation-driven feedback may instead facilitate LyC escape. The onset of SNe is expected to be delayed until $\sim 10 \text{ Myr}$ after a

star cluster’s birth (Jecmen & Oey 2023; Sukhbold et al. 2016), whereas the majority of known LCEs show 2 – 6 Myr-old stellar populations (Izotov et al. 2016a, 2018b; Saldana-Lopez et al. 2022). Stacking analysis by Flury et al. (2024) reveals that while older (> 8 Myr) stellar populations are ubiquitous among LCEs, but very young (< 3 Myr) populations are most important in the most prodigious LCEs. Galaxies with higher Ly α escape fractions may have slower velocities in LIS absorption lines tracing cold, neutral gas (Henry et al. 2015; Jaskot et al. 2017; Carr et al. 2021, 2024), suggesting weaker or suppressed mechanical feedback. Indeed, Carr et al. (2024) find that the strongest LyC leakers have lower mass, momentum, and energy loading in neutral gas. Stronger LCEs furthermore show flatter radio spectral indices indicative of a lack of non-thermal emission from SN feedback (Bait et al. 2024). In addition, the compactness and high gas densities characteristic of LyC-leaking starbursts may induce catastrophic radiative gas cooling, further diminishing the efficiency of any adiabatic superwinds (Silich et al. 2004; Gray et al. 2019). Direct evidence of catastrophic cooling such as nebular C IV $\lambda 1550$ emission is indeed seen to be associated with the extremely young SSC in Mrk 71-A (Oey et al. 2023), which additionally exhibits slow shell expansion velocities of ≤ 10 km s $^{-1}$ (Oey et al. 2017; Komarova et al. 2021); as mentioned earlier, this object is the nearest Green Pea analog and LCE candidate. Moreover, Pascale et al. (2023) present evidence for catastrophic cooling in the LyC-leaking knot of the Sunburst arc, where Mainali et al. (2022) report a wind component in nebular lines. Smith et al. (2023) suggest this knot is analogous to Mrk 71-A. Thus, radiation-driven feedback, rather than SN feedback, seems to be the dominant mode of LyC escape in the youngest, most extreme starbursts.

Instead, a new framework is emerging for LyC escape, based on studies of the largest sample of confirmed LCEs at low redshift, the LzLCS. There appear to be two classes of LCEs: one sub-sample shows relatively older ages, lower ionization, and higher metallicity (Flury et al. 2022b). The second group is characterized by extremely young ages, high O_{32} , and low metallicity, and on average higher $f_{\text{esc}}^{\text{LyC}}$ than the first group. These properties correspond to the radiation-dominated feedback described above. Indeed, stacking analysis of the LzLCS, in combination with 23 additional LCEs from the literature, shows that, while mechanical feedback is enhanced in LCEs compared to non-LCEs, the strongest leakers are dominated by < 3 Myr populations, too young for SN dominance (Flury et al. 2024). There is thus multifaceted evidence to support a new paradigm in which there are two regimes promoting the

escape of ionizing radiation from starbursts: one driven by SN feedback, and another by radiation-driven feedback.

Our study is consistent with this dual-mode paradigm for LyC escape. We suggest an additional way of distinguishing these two feedback modes by the morphology of the broad, $\lesssim 800$ km s $^{-1}$ emission-line wings that directly trace high-velocity ionized gas in very young, metal-poor systems. We present evidence showing that radiation-driven superwinds may be characteristic of the radiation-dominated mode, and are likely a key LyC escape mechanism in such objects as GPs, which are extremely young, highly ionized, and metal-poor starbursts. Conventional, SN-driven feedback still likely promotes LyC escape in older, more metal-rich populations. It remains to be determined whether superwinds generated by mechanical feedback can exhibit power-law nebular line wings, and if so, under what circumstances. But it is likely to be at significantly older ages in metal-poor galaxies (Jecmen & Oey 2023). In addition, prior SN feedback could still be important in reshaping the ISM and promoting LyC escape, even for the radiation-driven mode (Flury et al. 2024).

Radiation-driven superwinds may in fact be common at higher redshifts, where more starbursts are super-Eddington, promoting LyC and/or Ly α escape (Ferrara 2024). Such feedback may explain “blue monsters” at $z > 10$, where radiation-driven outflows clear dust efficiently (Ferrara et al. 2023; Ziparo et al. 2023). These massive early galaxies are predicted to have high star-formation efficiencies and thus lack mechanical feedback due to their free-fall times (~ 1 Myr) being shorter than the time required to develop stellar winds and SNe (Li et al. 2024; Dekel et al. 2023).

It is important to note that LyC escape may still occur via feedback modes not discussed in this work, such as in the case of the extreme LCE J1316+2614 with $f_{\text{esc}}^{\text{LyC}} \sim 90\%$ (Marques-Chaves et al. 2024), which shows no signatures of outflows. Instead, the efficient LyC escape may be explained by the high star-formation efficiency of $\geq 70\%$ in this object leading to density-bounded ionization.

5.2. Green Pea-Like Galaxies in the EoR

Our findings linking radiation-dominated feedback to LyC escape point to the possibility of a key role for GP-like galaxies in cosmic reionization. GPs are in fact defined by their compactness and exceptionally high ionization parameters (Cardamone et al. 2009; Amorín et al. 2012a; Fernández et al. 2022), which are directly linked to radiation-dominated gas kinematics (Yeh & Matzner 2012).

The first results from JWST are revealing that such extreme starbursts are abundant in the early universe (Rhoads et al. 2023; Mascia et al. 2023; Sanders et al. 2023; Simmonds et al. 2024a,b; Saxena et al. 2024), with even higher ionizing photon production efficiencies and lower metallicities (Arellano-Córdova et al. 2022; Schaerer et al. 2022; Matthee et al. 2023; Llerena et al. 2024; Castellano et al. 2024; Topping et al. 2024), as well as lower dust content (Cullen et al. 2024), than observed at low redshifts (Schaerer et al. 2022). In addition to enhanced ionizing photon production efficiencies, a stack of 1000 galaxies at $z = 4 - 10$ shows multiple signatures of strong LyC escape (Hayes et al. 2024). With higher ionization but delayed SN feedback due to the extremely low metallicities, these high-redshift galaxies likely have radiation-dominated stellar feedback. Indeed, broad emission-line wings have been detected in some of these objects with NIRCам wide field slitless spectroscopy and JWST/NIRSpec MSA spectroscopy (Xu et al. 2023; Matthee et al. 2023; Carniani et al. 2024; Saldana-Lopez et al. 2025).

6. CONCLUSION

Local LyC emitters, and in particular the most extreme starbursts such as Green Peas, exhibit high-velocity gas reaching 800 km s^{-1} in HWZI, observed as broad wings in emission lines of [O III] $\lambda 5007$ and H α . The velocity of this gas increases with the LyC escape fraction (Amorín et al. 2024), suggesting a direct link between stellar feedback and LyC leakage. These broad line wings may be able to identify the presence of radiation-driven superwinds, as seen in the nearest Green Pea analog Mrk 71-A, in which LyC photons impart their momentum on tiny, dense neutral knots, and a fraction of LyC escapes through their low filling factor (Komarova et al. 2021). We use our sample of 20 galaxies from the LzLCS survey (Flury et al. 2022a) and 6 GPs from the literature (Izotov et al. 2016a,b, 2018a,b) to determine the origin of the feedback traced by the broad emission-line wings. In particular, we test whether radiation-driven winds like that in Mrk 71-A are also responsible for the broad emission-line wings observed in these reionization-era analogs and whether they indeed promote LyC escape.

With spectroscopy from Magellan/MIKE, VLT/X-shooter, and WHT/ISIS, we determine the functional form or morphology of the broad-wing profile in [O III] $\lambda 5007$, as well as the wing maximum velocity, luminosity, systemic velocity, and other kinematic parameters, in each galaxy. We assume that the broad-wing morphology traces the dominant feedback regime in each starburst. As noted above, radiation-driven superwinds

produce line wings with power-law or exponential profiles (Krumholz et al. 2017; Komarova et al. 2021), whereas Gaussian profiles in young objects may be observed from unresolved regions dominated by mechanical feedback from SNe, where a large number of kinematic components obeys the central limit theorem (Chu & Kennicutt 1994).

We find that 14 out of the 26 sets of broad wings in our sample are better fit by power laws with slopes of -3.5 to -1.6 . Four other galaxies show Gaussian wings, and the remaining eight have ambiguous wing morphologies. We see that both Gaussian and power-law wing morphologies are found at lower $O_{32} < 3.5$, higher metallicities $12 + \log(\text{O}/\text{H}) > 8.0$, and moderate $\text{EW}(\text{H}\beta) < 75 \text{ \AA}$. However, the galaxies with higher O_{32} , lower $12 + \log(\text{O}/\text{H})$, and higher $\text{EW}(\text{H}\beta)$ all show non-Gaussian, power-law wings. In these extreme systems, such indicators of radiation feedback are linked to both the observed galaxy-wide properties and those of the broad-wing profiles such as wing luminosity and V_{max} . Objects with ambiguous wing morphologies show properties intermediate between those of the Gaussian and power-law classes.

We perform Kendall rank correlation tests for broad-wing parameters and galaxy properties in the power-law group. We find that the normalized wing luminosity at $\geq 300 \text{ km s}^{-1}$ $L_{\geq 300}/L_{\text{tot}}$ increases with the light fraction of stars younger than 3 Myr, $f_*(t < 3 \text{ Myr})$, suggesting that these youngest populations are responsible for radiation driving of the power-law wings, since the onset of SNe is not expected for ages $< 3 \text{ Myr}$, even at solar metallicity. Moreover, the power-law slope α is shallower for higher $f_*(t < 3 \text{ Myr})$, pointing to faster winds in younger populations. We also find that the normalized wing luminosity and α both correlate with the observed LyC luminosity $L_{\text{LyC,obs}}$ but not the LyC escape fraction $f_{\text{esc}}^{\text{LyC}}$. This suggests that *tracers of radiation-driven winds depend more on the driving UV luminosity than the covering fraction*. This is consistent with the wind and LyC photons emerging through the same optically thin channels in a picket-fence geometry (Heckman et al. 2001, 2011; Gazagnes et al. 2018; Steidel et al. 2018; Jaskot et al. 2019; Gazagnes et al. 2020; Saldana-Lopez et al. 2022). It also supports the scenario that radiation-driven superwinds modulate the LyC escape in the galaxies with power-law emission-line wings, and that higher LyC luminosities can accelerate faster winds.

We find that for galaxies with power-law slopes, the value of α appears to be determined not only by the intrinsic wind velocity profile as noted above, but also by extinction. We find that α_{red} is systematically shallower

than α_{blue} , with $\Delta\alpha \sim 0.5$ to 1.0 , with α_{red} becoming flatter for higher extinction. This implies a centrally concentrated dust distribution, either one that is spatially extended and strongly decreasing with radius, or a compact central dust zone limited to a smaller radius. Both of these configurations lead to preferential attenuation of the lower-velocity redshifted wind emission originating at smaller radii, which flattens the red slope. Additionally, α_{blue} trends with galaxy scaling relations, being flatter for galaxies that are, e.g., more metal-rich, and have lower O_{32} , SFR, $\text{EW}(\text{H}\beta)$ and $\text{EW}(\text{Ly}\alpha)$. The correlation of α_{blue} with absorbed LyC and extinction-linked properties is consistent with the first dust model and not the second.

Thus, both intrinsic wind structure and extinction appear to drive the observed values of α_{blue} and α_{red} , with extinction probing the geometry of the central, dusty region with respect to the wind velocity profile. We stress that extinction does *not* correlate with LyC escape in our data. Instead, there is a multi-dimensional relation whereby for a given $f_{\text{esc}}^{\text{LyC}}$, α flattens with extinction, while still showing trends of increasing LyC escape and flatter α with lower extinction. Our data remain consistent with previous findings that extinction anticorrelates with LyC escape.

We apparently find a systematic, redshifted offset between the broad-wing centroid velocity $V_{0,\text{wing}}$ and the narrow line core, with a median value of $\sim 19 \text{ km s}^{-1}$. This offset appears to be robust despite several factors that would bias the measurement in the opposite direction (see Section 4.5). The offset may result from a blueshifted line core emitted by a dense, expanding, momentum-conserving shell driven by weak stellar winds of the parent SSC, as seen in Mrk 71. This also could possibly be related to the similar observed offset of unknown origin between systemic Ly α emission and optical nebular lines in GPs (Orlitová et al. 2018).

We show that observed velocities in excess of 300 km s^{-1} are difficult to explain with dust opacity. Therefore, these winds are most likely accelerated by LyC and Ly α photons, as seen in Mrk 71-A (Komarova et al. 2021). The weak correlation between $f_{\text{esc}}^{\text{Ly}\alpha}$ and power-law slope suggests that LyC, rather than Ly α , radiation may dominate this process. This is reasonable, since Ly α is a resonant line that quickly rescatters, diluting its directional impact.

Using new Ly α imaging of a sub-sample of our galaxies with the LaCOS survey (Le Reste, in prep.), we see tentative evidence that more compact Ly α halos may be linked to broader emission-line wings. This may be expected given the $V_{\text{max}}-f_{\text{esc}}^{\text{LyC}}$ correlation, if stronger leak-

ers have less absorbed Ly α and lower global HI content, which lead to less Ly α scattering.

The galaxies with Gaussian broad wings, associated with higher metallicities and lower O_{32} values, are likely dominated by mechanical feedback from SNe. As evidenced by their lower O_{32} values and higher, though still subsolar, metallicities, these objects tend to be somewhat older, and more consistent with such a scenario.

Overall, our findings are consistent with the bimodal paradigm for LyC escape (e.g., Flury et al. 2024), now reinforced and clarified by observed emission-line wing profiles. These appear to be a powerful tracer of feedback and LyC escape mechanisms in very young starbursts: power-law wings mostly trace radiation-dominated superwinds, and Gaussian wings trace SN feedback. For systems with lower ionization parameters and higher metallicity, it remains somewhat unclear whether power-law wings could also result from SN-driven superwinds; in such cases, the timescale for developing a full-fledged superwind is critical. Another caveat is that our unresolved galaxies likely contain a multiplicity of star-forming regions with varying conditions, which limits the connections we can make between observed feedback properties and specific SSC parameters. These regions likely span a range of stellar ages, ionization parameters, metallicities, and both feedback modes may be present simultaneously.

We have shown that power-law emission-line wings have the potential to reveal fundamental parameters for the radiation-dominated conditions and feedback in individual objects. As JWST is uncovering extremely young, blue, metal-poor starbursts at $z > 6$, follow-up spectroscopic observations of such galaxies and their emission-line wings will help reveal the importance of radiation-driven feedback to LyC escape and to cosmic reionization.

1 We thank Mark Krumholz and Claus Leitherer for useful
 2 discussions. This work was supported by NASA grants
 3 HST-GO-16261.001 and HST-GO-17069.003 to M.S.O.
 4 R.A. and J.M.V. acknowledge financial support from
 5 the Severo Ochoa grant CEX2021-001131-S funded by
 6 MCIN/AEI/10.13039/501100011033. R.A. and J.M.V.
 7 acknowledge funding from projects PID2023-147386NB-
 8 I00 and PID2022- 136598NB-C32 “Estallidos8”, respec-
 9 tively. M.J.H. is fellow of the Knut & Alice Wallenberg
 10 Foundation. This work is based on observations with
 11 the NASA/ESA Hubble Space Telescope, which is oper-
 12 ated by the Association of Universities for Research in
 13 Astronomy, Incorporated, under NASA contract NAS5-
 14 26555. Support for Program numbers HST-GO-16261
 15 and HST-GO-17069 was provided through grants from
 16 the STScI under NASA contract NAS5-26555.

Facilities: HST/ACS,COS, Magellan/MIKE,
 VLT/X-shooter, WHT/ISIS

Software: Astropy (Astropy Collaboration et al.
 2022), SciPy (Virtanen et al. 2020), LMFIT (Newville
 et al. 2016), Matplotlib (Hunter 2007), kendall (Flury
 et al. 2022b).

REFERENCES

- Adamo, A., Östlin, G., Zackrisson, E., et al. 2010, MNRAS, 407, 870, doi: [10.1111/j.1365-2966.2010.16983.x](https://doi.org/10.1111/j.1365-2966.2010.16983.x)
- Akaike, H. 1974, IEEE Transactions on Automatic Control, 19, 716
- Akritas, M. G., & Siebert, J. 1996, MNRAS, 278, 919, doi: [10.1093/mnras/278.4.919](https://doi.org/10.1093/mnras/278.4.919)
- Amorín, R., Pérez-Montero, E., Vílchez, J. M., & Papaderos, P. 2012a, ApJ, 749, 185, doi: [10.1088/0004-637X/749/2/185](https://doi.org/10.1088/0004-637X/749/2/185)
- Amorín, R., Vílchez, J. M., Hägele, G. F., et al. 2012b, ApJL, 754, L22, doi: [10.1088/2041-8205/754/2/L22](https://doi.org/10.1088/2041-8205/754/2/L22)
- Amorín, R. O., Rodríguez-Henríquez, M., Fernández, V., et al. 2024, A&A, 682, L25, doi: [10.1051/0004-6361/202449175](https://doi.org/10.1051/0004-6361/202449175)
- Arellano-Córdova, K. Z., Berg, D. A., Chisholm, J., et al. 2022, ApJL, 940, L23, doi: [10.3847/2041-8213/ac9ab2](https://doi.org/10.3847/2041-8213/ac9ab2)
- Astropy Collaboration, Price-Whelan, A. M., Lim, P. L., et al. 2022, apj, 935, 167, doi: [10.3847/1538-4357/ac7c74](https://doi.org/10.3847/1538-4357/ac7c74)
- Atek, H., Labbé, I., Furtak, L. J., et al. 2024, Nature, 626, 975, doi: [10.1038/s41586-024-07043-6](https://doi.org/10.1038/s41586-024-07043-6)
- Bait, O., Borthakur, S., Schaerer, D., et al. 2024, A&A, 688, A198, doi: [10.1051/0004-6361/202348416](https://doi.org/10.1051/0004-6361/202348416)
- Baldwin, J. A., Phillips, M. M., & Terlevich, R. 1981, PASP, 93, 5, doi: [10.1086/130766](https://doi.org/10.1086/130766)
- Barrow, K. S. S., Robertson, B. E., Ellis, R. S., et al. 2020, ApJL, 902, L39, doi: [10.3847/2041-8213/abbd8e](https://doi.org/10.3847/2041-8213/abbd8e)
- Bernstein, R., Sheckman, S. A., Gunnels, S. M., Mochnacki, S., & Athey, A. E. 2003, in Society of Photo-Optical Instrumentation Engineers (SPIE) Conference Series, Vol. 4841, Instrument Design and Performance for Optical/Infrared Ground-based Telescopes, ed. M. Iye & A. F. M. Moorwood, 1694–1704, doi: [10.1117/12.461502](https://doi.org/10.1117/12.461502)
- Binette, L., Drissen, L., Úbeda, L., et al. 2009, A&A, 500, 817, doi: [10.1051/0004-6361/200811132](https://doi.org/10.1051/0004-6361/200811132)
- Björklund, R., Sundqvist, J. O., Singh, S. M., Puls, J., & Najarro, F. 2023, A&A, 676, A109, doi: [10.1051/0004-6361/202141948](https://doi.org/10.1051/0004-6361/202141948)
- Bosch, G., Hägele, G. F., Amorín, R., et al. 2019, MNRAS, 489, 1787, doi: [10.1093/mnras/stz2230](https://doi.org/10.1093/mnras/stz2230)
- Cardamone, C., Schawinski, K., Sarzi, M., et al. 2009, MNRAS, 399, 1191, doi: [10.1111/j.1365-2966.2009.15383.x](https://doi.org/10.1111/j.1365-2966.2009.15383.x)
- Carniani, S., Venturi, G., Parlanti, E., et al. 2024, A&A, 685, A99, doi: [10.1051/0004-6361/202347230](https://doi.org/10.1051/0004-6361/202347230)
- Carr, C., Scarlata, C., Henry, A., & Panagia, N. 2021, ApJ, 906, 104, doi: [10.3847/1538-4357/abc7c3](https://doi.org/10.3847/1538-4357/abc7c3)

- Carr, C. A., Cen, R., Scarlata, C., et al. 2024, arXiv e-prints, arXiv:2409.05180, doi: [10.48550/arXiv.2409.05180](https://doi.org/10.48550/arXiv.2409.05180)
- Castaneda, H. O., Vilchez, J. M., & Copetti, M. V. F. 1990, *ApJ*, 365, 164, doi: [10.1086/169466](https://doi.org/10.1086/169466)
- Castellano, M., Napolitano, L., Fontana, A., et al. 2024, *ApJ*, 972, 143, doi: [10.3847/1538-4357/ad5f88](https://doi.org/10.3847/1538-4357/ad5f88)
- Castor, J. I., Abbott, D. C., & Klein, R. I. 1975, *ApJ*, 195, 157, doi: [10.1086/153315](https://doi.org/10.1086/153315)
- Chemerynska, I., Atek, H., Dayal, P., et al. 2024, *ApJL*, 976, L15, doi: [10.3847/2041-8213/ad8dc9](https://doi.org/10.3847/2041-8213/ad8dc9)
- Chu, Y.-H., & Kennicutt, Robert C., J. 1994, *ApJ*, 425, 720, doi: [10.1086/174017](https://doi.org/10.1086/174017)
- Cristiani, S., Serrano, L. M., Fontanot, F., Vanzella, E., & Monaco, P. 2016, *MNRAS*, 462, 2478, doi: [10.1093/mnras/stw1810](https://doi.org/10.1093/mnras/stw1810)
- Crocker, R. M., Krumholz, M. R., Thompson, T. A., Baumgardt, H., & Mackey, D. 2018, *MNRAS*, 481, 4895, doi: [10.1093/mnras/sty2659](https://doi.org/10.1093/mnras/sty2659)
- Cullen, F., McLeod, D. J., McLure, R. J., et al. 2024, *MNRAS*, 531, 997, doi: [10.1093/mnras/stae1211](https://doi.org/10.1093/mnras/stae1211)
- Curti, M., D'Eugenio, F., Carniani, S., et al. 2023, *MNRAS*, 518, 425, doi: [10.1093/mnras/stac2737](https://doi.org/10.1093/mnras/stac2737)
- Danehar, A., Oey, M. S., & Gray, W. J. 2021, *ApJ*, 921, 91, doi: [10.3847/1538-4357/ac1a76](https://doi.org/10.3847/1538-4357/ac1a76)
- Dekel, A., Sarkar, K. C., Birnboim, Y., Mandelker, N., & Li, Z. 2023, *MNRAS*, 523, 3201, doi: [10.1093/mnras/stad1557](https://doi.org/10.1093/mnras/stad1557)
- Draine, B. T. 2003, *ARA&A*, 41, 241, doi: [10.1146/annurev.astro.41.011802.094840](https://doi.org/10.1146/annurev.astro.41.011802.094840)
- Duncan, K., & Conselice, C. J. 2015, *Monthly Notices of the Royal Astronomical Society*, 451, 2030, doi: [10.1093/mnras/stv1049](https://doi.org/10.1093/mnras/stv1049)
- Eggen, N. R., Scarlata, C., Skillman, E., & Jaskot, A. 2021, *ApJ*, 912, 12, doi: [10.3847/1538-4357/abe85d](https://doi.org/10.3847/1538-4357/abe85d)
- Fernández, V., Amorín, R., Pérez-Montero, E., et al. 2022, *MNRAS*, 511, 2515, doi: [10.1093/mnras/stab3150](https://doi.org/10.1093/mnras/stab3150)
- Ferrara, A. 2024, *A&A*, 684, A207, doi: [10.1051/0004-6361/202348321](https://doi.org/10.1051/0004-6361/202348321)
- Ferrara, A., Pallottini, A., & Dayal, P. 2023, *MNRAS*, 522, 3986, doi: [10.1093/mnras/stad1095](https://doi.org/10.1093/mnras/stad1095)
- Finkelstein, S. L., D'Aloisio, A., Paardekooper, J.-P., et al. 2019, *ApJ*, 879, 36, doi: [10.3847/1538-4357/ab1ea8](https://doi.org/10.3847/1538-4357/ab1ea8)
- Firpo, V., Bosch, G., Hägele, G. F., & Morrell, N. 2010, *MNRAS*, 406, 1094, doi: [10.1111/j.1365-2966.2010.16738.x](https://doi.org/10.1111/j.1365-2966.2010.16738.x)
- Flury, S. R., Moran, E. C., & Eleazer, M. 2023, *MNRAS*, 525, 4231, doi: [10.1093/mnras/stad2421](https://doi.org/10.1093/mnras/stad2421)
- Flury, S. R., Jaskot, A. E., Ferguson, H. C., et al. 2022a, *ApJS*, 260, 1, doi: [10.3847/1538-4365/ac5331](https://doi.org/10.3847/1538-4365/ac5331)
- . 2022b, *ApJ*, 930, 126, doi: [10.3847/1538-4357/ac61e4](https://doi.org/10.3847/1538-4357/ac61e4)
- Flury, S. R., Jaskot, A. E., Saldana-Lopez, A., et al. 2024, arXiv e-prints, arXiv:2409.12118, doi: [10.48550/arXiv.2409.12118](https://doi.org/10.48550/arXiv.2409.12118)
- Fontanot, F., Cristiani, S., & Vanzella, E. 2012, *MNRAS*, 425, 1413, doi: [10.1111/j.1365-2966.2012.21594.x](https://doi.org/10.1111/j.1365-2966.2012.21594.x)
- Gazagnes, S., Chisholm, J., Schaerer, D., Verhamme, A., & Izotov, Y. 2020, *A&A*, 639, A85, doi: [10.1051/0004-6361/202038096](https://doi.org/10.1051/0004-6361/202038096)
- Gazagnes, S., Chisholm, J., Schaerer, D., et al. 2018, *A&A*, 616, A29, doi: [10.1051/0004-6361/201832759](https://doi.org/10.1051/0004-6361/201832759)
- Gonzalez-Delgado, R. M., Perez, E., Tenorio-Tagle, G., et al. 1994, *ApJ*, 437, 239, doi: [10.1086/174992](https://doi.org/10.1086/174992)
- Gray, W. J., Oey, M. S., Silich, S., & Scannapieco, E. 2019, *ApJ*, 887, 161, doi: [10.3847/1538-4357/ab510d](https://doi.org/10.3847/1538-4357/ab510d)
- Grazian, A., Giallongo, E., Boutsia, K., et al. 2024, *ApJ*, 974, 84, doi: [10.3847/1538-4357/ad6980](https://doi.org/10.3847/1538-4357/ad6980)
- Guseva, N. G., Izotov, Y. I., Schaerer, D., et al. 2020, *MNRAS*, 497, 4293, doi: [10.1093/mnras/staa2197](https://doi.org/10.1093/mnras/staa2197)
- Hayes, M. J., Saldana-Lopez, A., Citro, A., et al. 2024, arXiv e-prints, arXiv:2411.09262, doi: [10.48550/arXiv.2411.09262](https://doi.org/10.48550/arXiv.2411.09262)
- He, X., Wang, X., Jones, T., et al. 2024, *ApJL*, 960, L13, doi: [10.3847/2041-8213/ad12cd](https://doi.org/10.3847/2041-8213/ad12cd)
- Heckman, T. M., Sembach, K. R., Meurer, G. R., et al. 2001, *ApJ*, 558, 56, doi: [10.1086/322475](https://doi.org/10.1086/322475)
- Heckman, T. M., Borthakur, S., Overzier, R., et al. 2011, *ApJ*, 730, 5, doi: [10.1088/0004-637X/730/1/5](https://doi.org/10.1088/0004-637X/730/1/5)
- Heger, A., Fryer, C. L., Woosley, S. E., Langer, N., & Hartmann, D. H. 2003, *ApJ*, 591, 288, doi: [10.1086/375341](https://doi.org/10.1086/375341)
- Henry, A., Scarlata, C., Martin, C. L., & Erb, D. 2015, *ApJ*, 809, 19, doi: [10.1088/0004-637X/809/1/19](https://doi.org/10.1088/0004-637X/809/1/19)
- Hogarth, L., Amorín, R., Vilchez, J. M., et al. 2020, *MNRAS*, 494, 3541, doi: [10.1093/mnras/staa851](https://doi.org/10.1093/mnras/staa851)
- Hunter, J. D. 2007, *Computing in Science & Engineering*, 9, 90, doi: [10.1109/MCSE.2007.55](https://doi.org/10.1109/MCSE.2007.55)
- Ishibashi, W., & Fabian, A. C. 2015, *MNRAS*, 451, 93, doi: [10.1093/mnras/stv944](https://doi.org/10.1093/mnras/stv944)
- Izotov, Y. I., Orlitová, I., Schaerer, D., et al. 2016a, *Nature*, 529, 178, doi: [10.1038/nature16456](https://doi.org/10.1038/nature16456)
- Izotov, Y. I., Schaerer, D., Thuan, T. X., et al. 2016b, *MNRAS*, 461, 3683, doi: [10.1093/mnras/stw1205](https://doi.org/10.1093/mnras/stw1205)
- Izotov, Y. I., Schaerer, D., Worseck, G., et al. 2018a, *MNRAS*, 474, 4514, doi: [10.1093/mnras/stx3115](https://doi.org/10.1093/mnras/stx3115)
- Izotov, Y. I., Thuan, T. X., & Lipovetsky, V. A. 1997, *ApJS*, 108, 1, doi: [10.1086/312956](https://doi.org/10.1086/312956)
- Izotov, Y. I., Worseck, G., Schaerer, D., et al. 2018b, *MNRAS*, 478, 4851, doi: [10.1093/mnras/sty1378](https://doi.org/10.1093/mnras/sty1378)

- Jaskot, A. E., Dowd, T., Oey, M. S., Scarlata, C., & McKinney, J. 2019, *ApJ*, 885, 96, doi: [10.3847/1538-4357/ab3d3b](https://doi.org/10.3847/1538-4357/ab3d3b)
- Jaskot, A. E., & Oey, M. S. 2013, *ApJ*, 766, 91, doi: [10.1088/0004-637X/766/2/91](https://doi.org/10.1088/0004-637X/766/2/91)
- Jaskot, A. E., Oey, M. S., Scarlata, C., & Dowd, T. 2017, *ApJL*, 851, L9, doi: [10.3847/2041-8213/aa9d83](https://doi.org/10.3847/2041-8213/aa9d83)
- Jecmen, M. C., & Oey, M. S. 2023, *ApJ*, 958, 149, doi: [10.3847/1538-4357/ad0460](https://doi.org/10.3847/1538-4357/ad0460)
- Keenan, R. P., Oey, M. S., Jaskot, A. E., & James, B. L. 2017, *The Astrophysical Journal*, 848, 12, doi: [10.3847/1538-4357/aa8b77](https://doi.org/10.3847/1538-4357/aa8b77)
- Kelson, D. D. 2003, *PASP*, 115, 688, doi: [10.1086/375502](https://doi.org/10.1086/375502)
- Kelson, D. D., Illingworth, G. D., van Dokkum, P. G., & Franx, M. 2000, *ApJ*, 531, 159, doi: [10.1086/308445](https://doi.org/10.1086/308445)
- Kimm, T., & Cen, R. 2014, *ApJ*, 788, 121, doi: [10.1088/0004-637X/788/2/121](https://doi.org/10.1088/0004-637X/788/2/121)
- Komarova, L. 2024, PhD thesis, University of Michigan. <https://proxy.lib.umich.edu/login?url=https://www.proquest.com/dissertations-theses/local-starbursts-reionization-radiation-driven/docview/3152012089/se-2>
- Komarova, L., Oey, M. S., Krumholz, M. R., et al. 2021, *ApJL*, 920, L46, doi: [10.3847/2041-8213/ac2c09](https://doi.org/10.3847/2041-8213/ac2c09)
- Komarova, L., Oey, M. S., Hernandez, S., et al. 2024, *ApJ*, 967, 117, doi: [10.3847/1538-4357/ad3962](https://doi.org/10.3847/1538-4357/ad3962)
- Krumholz, M. R., Thompson, T. A., Ostriker, E. C., & Martin, C. L. 2017, *MNRAS*, 471, 4061, doi: [10.1093/mnras/stx1882](https://doi.org/10.1093/mnras/stx1882)
- Kunth, D., Leitherer, C., Mas-Hesse, J. M., Östlin, G., & Petrosian, A. 2003, *ApJ*, 597, 263, doi: [10.1086/378396](https://doi.org/10.1086/378396)
- Le Reste, A., Cannon, J. M., Hayes, M. J., et al. 2024, *MNRAS*, 528, 757, doi: [10.1093/mnras/stad3910](https://doi.org/10.1093/mnras/stad3910)
- Leitherer, C., Ekström, S., Meynet, G., et al. 2014, *ApJS*, 212, 14, doi: [10.1088/0067-0049/212/1/14](https://doi.org/10.1088/0067-0049/212/1/14)
- Li, Z., Dekel, A., Sarkar, K. C., et al. 2024, *A&A*, 690, A108, doi: [10.1051/0004-6361/202348727](https://doi.org/10.1051/0004-6361/202348727)
- Llerena, M., Amorín, R., Pentericci, L., et al. 2024, *A&A*, 691, A59, doi: [10.1051/0004-6361/202449904](https://doi.org/10.1051/0004-6361/202449904)
- Lochhaas, C., & Thompson, T. A. 2017, *MNRAS*, 470, 977, doi: [10.1093/mnras/stx1289](https://doi.org/10.1093/mnras/stx1289)
- Ma, X., Kasen, D., Hopkins, P. F., et al. 2015, *MNRAS*, 453, 960, doi: [10.1093/mnras/stv1679](https://doi.org/10.1093/mnras/stv1679)
- Ma, X., Quataert, E., Wetzel, A., et al. 2020, *MNRAS*, 498, 2001, doi: [10.1093/mnras/staa2404](https://doi.org/10.1093/mnras/staa2404)
- Mainali, R., Rigby, J. R., Chisholm, J., et al. 2022, *ApJ*, 940, 160, doi: [10.3847/1538-4357/ac9cd6](https://doi.org/10.3847/1538-4357/ac9cd6)
- Marques-Chaves, R., Schaerer, D., Amorín, R. O., et al. 2022, *A&A*, 663, L1, doi: [10.1051/0004-6361/202243598](https://doi.org/10.1051/0004-6361/202243598)
- Marques-Chaves, R., Schaerer, D., Vanzella, E., et al. 2024, *A&A*, 691, A87, doi: [10.1051/0004-6361/202451667](https://doi.org/10.1051/0004-6361/202451667)
- Mascia, S., Pentericci, L., Calabrò, A., et al. 2023, *A&A*, 672, A155, doi: [10.1051/0004-6361/202345866](https://doi.org/10.1051/0004-6361/202345866)
- Matsuoka, Y., Strauss, M. A., Kashikawa, N., et al. 2018, *ApJ*, 869, 150, doi: [10.3847/1538-4357/aace7a](https://doi.org/10.3847/1538-4357/aace7a)
- Matthee, J., Mackenzie, R., Simcoe, R. A., et al. 2023, *ApJ*, 950, 67, doi: [10.3847/1538-4357/acc846](https://doi.org/10.3847/1538-4357/acc846)
- Matthee, J., Naidu, R. P., Pezzulli, G., et al. 2022, *MNRAS*, 512, 5960, doi: [10.1093/mnras/stac801](https://doi.org/10.1093/mnras/stac801)
- McClymont, W., Tacchella, S., D'Eugenio, F., et al. 2024, arXiv e-prints, arXiv:2405.15859, doi: [10.48550/arXiv.2405.15859](https://doi.org/10.48550/arXiv.2405.15859)
- McKinney, J. H., Jaskot, A. E., Oey, M. S., et al. 2019, *ApJ*, 874, 52, doi: [10.3847/1538-4357/ab08eb](https://doi.org/10.3847/1538-4357/ab08eb)
- Micheva, G., Oey, M. S., Jaskot, A. E., & James, B. L. 2017, *ApJ*, 845, 165, doi: [10.3847/1538-4357/aa830b](https://doi.org/10.3847/1538-4357/aa830b)
- Naidu, R. P., Tacchella, S., Mason, C. A., et al. 2020, *ApJ*, 892, 109, doi: [10.3847/1538-4357/ab7cc9](https://doi.org/10.3847/1538-4357/ab7cc9)
- Nakajima, K., Ouchi, M., Isobe, Y., et al. 2023, *ApJS*, 269, 33, doi: [10.3847/1538-4365/acd556](https://doi.org/10.3847/1538-4365/acd556)
- Newville, M., Stensitzki, T., Allen, D. B., & Ingargiola, A. 2014, LMFIT: Non-Linear Least-Square Minimization and Curve-Fitting for Python, 0.8.0, Zenodo, doi: [10.5281/zenodo.11813](https://doi.org/10.5281/zenodo.11813)
- Newville, M., Stensitzki, T., Allen, D. B., et al. 2016, Lmfit: Non-Linear Least-Square Minimization and Curve-Fitting for Python, Astrophysics Source Code Library, record ascl:1606.014. <http://ascl.net/1606.014>
- O'Connor, E., & Ott, C. D. 2011, *ApJ*, 730, 70, doi: [10.1088/0004-637X/730/2/70](https://doi.org/10.1088/0004-637X/730/2/70)
- Oey, M. S., Herrera, C. N., Silich, S., et al. 2017, *ApJL*, 849, L1, doi: [10.3847/2041-8213/aa9215](https://doi.org/10.3847/2041-8213/aa9215)
- Oey, M. S., Sawant, A. N., Danehkar, A., et al. 2023, *ApJL*, 958, L10, doi: [10.3847/2041-8213/ad07dd](https://doi.org/10.3847/2041-8213/ad07dd)
- Orlitová, I., Verhamme, A., Henry, A., et al. 2018, *A&A*, 616, A60, doi: [10.1051/0004-6361/201732478](https://doi.org/10.1051/0004-6361/201732478)
- Östlin, G., Rivera-Thorsen, T. E., Menacho, V., et al. 2021, *ApJ*, 912, 155, doi: [10.3847/1538-4357/abf1e8](https://doi.org/10.3847/1538-4357/abf1e8)
- Pascale, M., Dai, L., McKee, C. F., & Tsang, B. T. H. 2023, *ApJ*, 957, 77, doi: [10.3847/1538-4357/acf75c](https://doi.org/10.3847/1538-4357/acf75c)
- Petrosian, V. 1976, *ApJL*, 210, L53, doi: [10.1086/18230110.1086/182253](https://doi.org/10.1086/18230110.1086/182253)
- Ramachandran, V., Hamann, W. R., Oskinova, L. M., et al. 2019, *A&A*, 625, A104, doi: [10.1051/0004-6361/201935365](https://doi.org/10.1051/0004-6361/201935365)
- Reddy, N. A., Steidel, C. C., Pettini, M., Bogosavljević, M., & Shapley, A. E. 2016, *ApJ*, 828, 108, doi: [10.3847/0004-637X/828/2/108](https://doi.org/10.3847/0004-637X/828/2/108)

- Rhoads, J. E., Wold, I. G. B., Harish, S., et al. 2023, *ApJL*, 942, L14, doi: [10.3847/2041-8213/acaaf](https://doi.org/10.3847/2041-8213/acaaf)
- Rickard, M. J., Hainich, R., Hamann, W. R., et al. 2022, *A&A*, 666, A189, doi: [10.1051/0004-6361/202243281](https://doi.org/10.1051/0004-6361/202243281)
- Robertson, B. E., Ellis, R. S., Furlanetto, S. R., & Dunlop, J. S. 2015, *ApJL*, 802, L19, doi: [10.1088/2041-8205/802/2/L19](https://doi.org/10.1088/2041-8205/802/2/L19)
- Robertson, B. E., Furlanetto, S. R., Schneider, E., et al. 2013, *ApJ*, 768, 71, doi: [10.1088/0004-637X/768/1/71](https://doi.org/10.1088/0004-637X/768/1/71)
- Rodriguez-Gomez, V., Snyder, G. F., Lotz, J. M., et al. 2019, *MNRAS*, 483, 4140, doi: [10.1093/mnras/sty3345](https://doi.org/10.1093/mnras/sty3345)
- Rosado, M., Laval, A., Le Coarer, E., et al. 1996, *A&A*, 308, 588
- Roy, J.-R., Boulesteix, J., Joncas, G., & Grundseth, B. 1991, *ApJ*, 367, 141, doi: [10.1086/169609](https://doi.org/10.1086/169609)
- Saldana-Lopez, A., Schaerer, D., Chisholm, J., et al. 2022, *A&A*, 663, A59, doi: [10.1051/0004-6361/202141864](https://doi.org/10.1051/0004-6361/202141864)
- Saldana-Lopez, A., Chisholm, J., Gazagnes, S., et al. 2025, *arXiv e-prints*, arXiv:2501.17145, doi: [10.48550/arXiv.2501.17145](https://doi.org/10.48550/arXiv.2501.17145)
- Sanders, R. L., Shapley, A. E., Clarke, L., et al. 2023, *ApJ*, 943, 75, doi: [10.3847/1538-4357/aca9cc](https://doi.org/10.3847/1538-4357/aca9cc)
- Saxena, A., Bunker, A. J., Jones, G. C., et al. 2024, *A&A*, 684, A84, doi: [10.1051/0004-6361/202347132](https://doi.org/10.1051/0004-6361/202347132)
- Schaerer, D., Marques-Chaves, R., Barrufet, L., et al. 2022, *A&A*, 665, L4, doi: [10.1051/0004-6361/202244556](https://doi.org/10.1051/0004-6361/202244556)
- Schneider, E. E., & Mao, S. A. 2024, *ApJ*, 966, 37, doi: [10.3847/1538-4357/ad2e8a](https://doi.org/10.3847/1538-4357/ad2e8a)
- Schneider, E. E., Ostriker, E. C., Robertson, B. E., & Thompson, T. A. 2020, *ApJ*, 895, 43, doi: [10.3847/1538-4357/ab8ae8](https://doi.org/10.3847/1538-4357/ab8ae8)
- Shopbell, P. L., & Bland-Hawthorn, J. 1998, *ApJ*, 493, 129, doi: [10.1086/305108](https://doi.org/10.1086/305108)
- Silich, S., Tenorio-Tagle, G., & Rodríguez-González, A. 2004, *ApJ*, 610, 226, doi: [10.1086/421702](https://doi.org/10.1086/421702)
- Simmonds, C., Tacchella, S., Hainline, K., et al. 2024a, *MNRAS*, 527, 6139, doi: [10.1093/mnras/stad3605](https://doi.org/10.1093/mnras/stad3605)
- . 2024b, *MNRAS*, 535, 2998, doi: [10.1093/mnras/stae2537](https://doi.org/10.1093/mnras/stae2537)
- Smith, L. J., Oey, M. S., Hernandez, S., et al. 2023, *ApJ*, 958, 194, doi: [10.3847/1538-4357/ad00b4](https://doi.org/10.3847/1538-4357/ad00b4)
- Steidel, C. C., Bogosavljević, M., Shapley, A. E., et al. 2018, *ApJ*, 869, 123, doi: [10.3847/1538-4357/aaed28](https://doi.org/10.3847/1538-4357/aaed28)
- Sukhbold, T., Ertl, T., Woosley, S. E., Brown, J. M., & Janka, H. T. 2016, *ApJ*, 821, 38, doi: [10.3847/0004-637X/821/1/38](https://doi.org/10.3847/0004-637X/821/1/38)
- Thompson, T. A., Fabian, A. C., Quataert, E., & Murray, N. 2015, *MNRAS*, 449, 147, doi: [10.1093/mnras/stv246](https://doi.org/10.1093/mnras/stv246)
- Thompson, T. A., & Krumholz, M. R. 2016, *MNRAS*, 455, 334, doi: [10.1093/mnras/stv2331](https://doi.org/10.1093/mnras/stv2331)
- Tolstoy, E., Saha, A., Hoessel, J. G., & McQuade, K. 1995, *AJ*, 110, 1640, doi: [10.1086/117637](https://doi.org/10.1086/117637)
- Tomaselli, G. M., & Ferrara, A. 2021, *MNRAS*, 504, 89, doi: [10.1093/mnras/stab876](https://doi.org/10.1093/mnras/stab876)
- Topping, M. W., Stark, D. P., Senchyna, P., et al. 2024, *MNRAS*, 529, 3301, doi: [10.1093/mnras/stae682](https://doi.org/10.1093/mnras/stae682)
- Torres-Flores, S., Barbá, R., Maíz Apellániz, J., et al. 2013, *A&A*, 555, A60, doi: [10.1051/0004-6361/201220474](https://doi.org/10.1051/0004-6361/201220474)
- Trebitsch, M., Blaizot, J., Rosdahl, J., Devriendt, J., & Slyz, A. 2017, *MNRAS*, 470, 224, doi: [10.1093/mnras/stx1060](https://doi.org/10.1093/mnras/stx1060)
- Ulivi, L., Venturi, G., Cresci, G., et al. 2024, *A&A*, 685, A122, doi: [10.1051/0004-6361/202347436](https://doi.org/10.1051/0004-6361/202347436)
- Vink, J. S., de Koter, A., & Lamers, H. J. G. L. M. 2001, *A&A*, 369, 574, doi: [10.1051/0004-6361:20010127](https://doi.org/10.1051/0004-6361:20010127)
- Virtanen, P., Gommers, R., Oliphant, T. E., et al. 2020, *Nature Methods*, 17, 261, doi: [10.1038/s41592-019-0686-2](https://doi.org/10.1038/s41592-019-0686-2)
- Škoda, P., Šurlan, B., & Tomić, S. 2008, in *Society of Photo-Optical Instrumentation Engineers (SPIE) Conference Series*, Vol. 7014, *Ground-based and Airborne Instrumentation for Astronomy II*, ed. I. S. McLean & M. M. Casali, 70145X, doi: [10.1117/12.789284](https://doi.org/10.1117/12.789284)
- Xu, X., Henry, A., Heckman, T., et al. 2024, *arXiv e-prints*, arXiv:2409.19776, doi: [10.48550/arXiv.2409.19776](https://doi.org/10.48550/arXiv.2409.19776)
- Xu, Y., Ouchi, M., Nakajima, K., et al. 2023, *arXiv e-prints*, arXiv:2310.06614, doi: [10.48550/arXiv.2310.06614](https://doi.org/10.48550/arXiv.2310.06614)
- Yeh, J. Y. C., Smith, A., Kannan, R., et al. 2023, *MNRAS*, 520, 2757, doi: [10.1093/mnras/stad210](https://doi.org/10.1093/mnras/stad210)
- Yeh, S. C. C., & Matzner, C. D. 2012, *ApJ*, 757, 108, doi: [10.1088/0004-637X/757/2/108](https://doi.org/10.1088/0004-637X/757/2/108)
- Zackrisson, E., Inoue, A. K., & Jensen, H. 2013, *ApJ*, 777, 39, doi: [10.1088/0004-637X/777/1/39](https://doi.org/10.1088/0004-637X/777/1/39)
- Zastrow, J., Oey, M. S., Veilleux, S., & McDonald, M. 2013, *ApJ*, 779, 76, doi: [10.1088/0004-637X/779/1/76](https://doi.org/10.1088/0004-637X/779/1/76)
- Zhang, W., Woosley, S. E., & Heger, A. 2008, *ApJ*, 679, 639, doi: [10.1086/526404](https://doi.org/10.1086/526404)
- Ziparo, F., Ferrara, A., Sommovigo, L., & Kohandel, M. 2023, *MNRAS*, 520, 2445, doi: [10.1093/mnras/stad125](https://doi.org/10.1093/mnras/stad125)